Restoring Oscillatory Dynamics in Alzheimer's Disease: A Laminar Whole-Brain Model of Serotonergic Psychedelic Effects

Jan C. Gendra[1,2,4,*], Edmundo Lopez-Sola[1,3,*], Francesca Castaldo[1], Èlia Lleal-Custey[1], Roser Sanchez-Todo[1,3], Jakub Vohryzek[3], Ricardo Salvador[1], Ralph G. Andrzejak[2], and Giulio Ruffini[1,**], for the Alzheimer's Disease Neuroimaging Initiative

[1]Brain Modeling Department, Neuroelectrics, Barcelona, Spain
[2]Department of Engineering, Universitat Pompeu Fabra, Barcelona, Spain
[3]Center for Brain and Cognition, Universitat Pompeu Fabra, Barcelona, Spain
[4]School of Computation, Information and Technology, Technical University of Munich, Munich, Germany

Abstract

Classical serotonergic psychedelics show promise in addressing neurodegenerative disorders such as Alzheimer's disease by modulating pathological brain dynamics. However, the precise neurobiological mechanisms underlying their effects remain elusive. This study introduces a personalized whole-brain model built upon a laminar neural mass framework to elucidate these effects. Using multimodal neuroimaging data from thirty subjects diagnosed with Alzheimer's disease, we simulate the impact of serotonin 2A receptor activation, characteristic of psychedelics, on cortical dynamics. By modulating the excitability of layer 5 pyramidal neurons, our models reproduce hallmark changes in EEG power spectra observed under psychedelics, including alpha power suppression and gamma power enhancement. These spectral shifts are shown to correlate strongly with the regional distribution of serotonin 2A receptors. Furthermore, simulated EEG reveals increased complexity and entropy, suggesting restored network function. These findings underscore the potential of serotonergic psychedelics to reestablish healthy oscillatory dynamics in the prodromal and early phases of Alzheimer's disease and offer mechanistic insights into their potential therapeutic effects in neurodegenerative disorders.

---

*Equal contribution

**Corresponding Author: giulio.ruffini@neuroelectrics.com (G. Ruffini)

† Data used in the preparation of this article were obtained from the Alzheimer's Disease Neuroimaging Initiative (ADNI) database (http://adni.loni.usc.edu). As such, the investigators within the ADNI contributed to the design and implementation of ADNI and/or provided data but did not participate in the analysis or writing of this report. A complete listing of ADNI investigators can be found at: http://adni.loni.usc.edu/wp-content/uploads/how_to_apply/ADNI_Acknowledgement_List.pdf

Keywords: Psychedelics, Alzheimer's disease, Neuropsychiatry, Serotonin, 5-HT2A, PET, Whole-Brain Model, Laminar Neural Mass Model, fMRI, EEG

Index

1 Introduction **1**

2 Methods **3**
2.1 Laminar model of the effects of psychedelics 3
2.2 Baseline AD whole-brain models 5
2.3 Whole-brain models under psychedelics 7
2.4 Simulation of EEG recordings using hybrid brain models 8
2.5 Complexity and entropy of simulated EEG 9

3 Results **10**
3.1 Uncoupled LaNMM spectral profile 10
3.2 Whole-brain model personalization 11
3.3 Whole-brain spectral profile under psychedelics 13
3.4 Influence of 5-HT2AR distribution on oscillatory activity 15
3.5 Model-generated EEG alpha and gamma power 16
3.6 Simulated EEG complexity and entropy 17

4 Discussion **17**
4.1 Main findings 17
4.2 Potential therapeutic role of psychedelics in AD 19
4.3 Limitations and future work 20

5 Conclusions **20**

Supplementary Information **34**

1 Introduction

In the last couple of decades, classical serotonergic psychedelics (hereby, *psychedelics*) have re-emerged as potential treatments for a range of different neuropsychiatric disorders, yielding promising results.[1–3] Emerging evidence also points to the potential of psychedelics in treating neurodegenerative conditions, such as Alzheimer's disease (AD) and related dementias.[4–7] While current evidence is primarily preclinical, there is growing interest in investigating psychedelics as potential treatments for AD, with both high-dose and micro-dosing regimens being considered.[5,6]

Serotonergic psychedelics primarily act as agonists of the serotonin 2A receptor (5-HT2AR),[1,3,8,9] though other receptors, such as 5-HT1AR, may also contribute to these effects.[10,11] The intensity of these effects is linked to the degree of occupancy of these receptors.[12] Among the different serotonin receptor (5-HT) subtypes, 5-HT2ARs are the most abundant in the cortex[13] and show some regional heterogeneity.[1,14,15] 5-HT2A receptors modulate the excitatory effects of glutamate, particularly by enhancing the excitability of deep-layer pyramidal neurons to glutamate inputs (i.e., making them more susceptible to excitatory inputs typically associated with glutamate receptors).[15] This enhanced excitation dysregulates the spontaneous activity in cortical populations, increasing the entropy or complexity of ongoing brain activity and producing alterations in its power spectrum.[1,8] In particular, the power changes associated with 5-HT2AR activation disrupt the brain's normal alpha rhythm dynamics, resulting in a widespread decrease in the mean power spectral density (PSD) of the alpha band in the cortex[1,8,16–18] and an increase in the cortical gamma band power.[18,19]

These mechanisms may be particularly valuable in the context of Alzheimer's disease, where disrupted oscillatory patterns, reduced complexity, and impaired connectivity are hallmarks of the disorder. Specifically, these disruptions evolve across the stages of the disease, reflecting progressive impairments in neural dynamics. During the preclinical phase, alpha activity is disrupted,[20,21] while gamma power shows variability, with reports of increases, stability, or reductions.[22,23] As the disease progresses into the prodromal phase, alpha power remains elevated.[20] During this phase, gamma power is thought to decline due to the dysfunction of parvalbumin (PV) interneurons, which are essential for generating gamma oscillations and maintaining network balance.[24,25] However, some studies report increased gamma power instead.[26] In the mild to moderate stages, alpha power declines, gamma power becomes markedly reduced, and neural complexity decreases, reflecting growing impairments in synaptic function, network flexibility, and cognitive processing.[27–29] For a more detailed discussion of AD physiopathology and oscillatory deficits, see Appendix S.1.

Psychedelics, acting through the mechanisms described above, could counteract these deficits by reducing alpha power, thereby alleviating hyper-synchronization and enhancing network flexibility. Their ability to increase gamma power is particularly relevant for addressing PV interneuron dysfunction, potentially restoring gamma oscillations and rebalancing excitatory-inhibitory networks.[25,30] Additionally, psychedelics enhance neural complexity, increasing entropy and promoting a

Table 1: Compensation of AD deficits by serotonergic psychedelics, which suggest potential therapeutic value in early AD.

Feature	AD Deficit	Compensation by psychedelics
Alpha Power	Increased alpha power and alpha hypersynchronization (preclinical and prodromal);[20,21,33] eventual decrease in alpha peak frequency and alpha power in later stages.[34–36]	Psychedelics reduce alpha power, increasing network flexibility and interconnectivity.[1,8,37] Potentially valuable in early AD.
Gamma Power	Possible preclinical increases in gamma,[22] decreased gamma activity in prodromal and later stages,[24] impairing cognitive processes and memory.[25]	Psychedelics increase gamma power, promoting oscillations associated with cognitive processing.[18,19,37] Potentially valuable after preclinical phase.
Delta and Theta Power	Increased power in delta and theta bands; hypersynchrony in slow oscillations.[20,26,34]	Psychedelics reduce delta and theta power, countering hypersynchrony and restoring balance across frequencies.[38]
Complexity	Decreased entropy and complexity of brain activity.[28]	Psychedelics increase entropy and brain signal complexity.[1,31,32,39]
Inhibitory-Excitatory Balance	Impaired PV interneuron function disrupts gamma oscillations and leads to network instability.[25]	Psychedelics engage 5-HT2AR on pyramidal neurons, indirectly improving PV interneuron function and rebalancing excitatory-inhibitory networks.[30]
Network Features	Decreased global connectivity and increased modularity; network decoupling.[40]	Psychedelics increase global functional connectivity and reduce modularity, promoting integration and flexibility.[41]

more flexible and integrated network state,[1,31,32] which may help counteract the rigidity and loss of complexity observed in Alzheimer's disease. These effects suggest that psychedelics could be especially effective in the prodromal and mild stages of the disease, where compensatory mechanisms remain active, and neural circuits are less extensively damaged. A summary of how psychedelics may compensate for these deficits in AD is presented in Table 1.

A deeper understanding of the mechanisms underlying the effects of psychedelics is essential to develop such effective treatments.[1,3,8] Psychedelics affect brain dynamics across scales, from subcellular mechanisms to whole-brain networks, making computational models valuable tools for exploring their therapeutic potential. Such mechanistic models have recently proven helpful in advancing our understanding of the mechanism of action of psychedelics.[42–49] However, existing computational models primarily focus on macroscale brain dynamics, overlooking critical mesoscale and microscale dynamics, such as neuronal population interactions that mediate oscillatory changes. Moreover, there is a notable lack of computational studies examining the effects of psychedelics in the context of AD.

Mesoscale modeling may be well suited to reproduce such oscillatory alterations by psychedelics in AD, as it represents an intermediate level between the macro- and micro-scale and focuses on neuronal populations and local circuits within brain regions. Computational approaches such as neural mass models (NMMs) and neural field models are frequently used in mesoscale modeling to simulate the collective behavior of neuronal populations.[50,51] The laminar NMM (LaNMM) framework is a natural extension of the neural mass formalism to produce coupled fast (gamma)

and slow (alpha) oscillatory activity and simulate realistic electrophysiological signals.[52,53] It has been recently applied in the context of AD,[54] showing how disrupted PV-to-pyramidal connectivity can explain the PSD alterations observed in the process of neurodegeneration in AD. By capturing multiband oscillatory dynamics, the LaNMM provides a unique framework for modeling neuronal processes in conditions like AD or under exposure to psychedelics, where disruptions in slow and fast oscillatory activity are prominent.

Furthermore, most of the current macroscale models of psychedelics do not include a realistic biophysical medium, making it challenging to align their outputs with electrophysiological measurements such as scalp electroencephalography (EEG) or magnetoencephalography (MEG), typically used in experimental studies. This discrepancy hinders the potential of these models for *in silico* validation of empirical data and testing of treatments for neuropsychiatric disorders.[55] Hybrid brain models (HBMs),[56,57] which combine physiological and biophysical information of the brain, address this gap by integrating multimodal subject-specific data and simulating realistic physiological outputs.

In this study, we investigate the effects of psychedelics at the whole-brain level and their therapeutic potential in AD using the biophysically realistic LaNMM. With multimodal data from a cohort of AD subjects, we create personalized hybrid brain models based on the LaNMM. We hypothesize that such whole-brain models can reproduce the changes in the power spectrum of the brain's neuronal activity recorded via local field or scalp potentials associated with the known effects of psychedelics (and with the therapeutic potential for AD), including a marked decrease in alpha oscillations and an increase of gamma oscillations.

2 Methods

The present study aims to provide new insights into the mechanisms of psychedelic action and its effects on the brain's spontaneous activity by studying the mechanisms behind the spectral power alterations under the acute phase of psychedelics. For this purpose, we a) develop a laminar neural mass modeling framework integrating the effects of psychedelics that reproduces the multiband PSD changes in the neural activity of a cortical column, b) generate subject-specific whole-brain models based on diffusion magnetic resonance imaging (dMRI) and functional MRI (fMRI) data from AD subjects, c) integrate the effects of psychedelics following a positron emission tomography (PET)-informed distribution of 5-HT2AR densities and study the effects of psychedelics at the whole-brain level in the cohort of AD subjects, and d) combine such whole-brain models with a biophysical layer to simulate realistic electrophysiological activity (i.e., EEG) under psychedelics. An overview of the methodology followed in this study is shown in Figure 1.

2.1 Laminar model of the effects of psychedelics

The LaNMM consists of two coupled neural masses—a Jansen-Rit (JR)[50] and a pyramidal-interneuron-gamma (PING) model[58]— to simulate both slow and fast

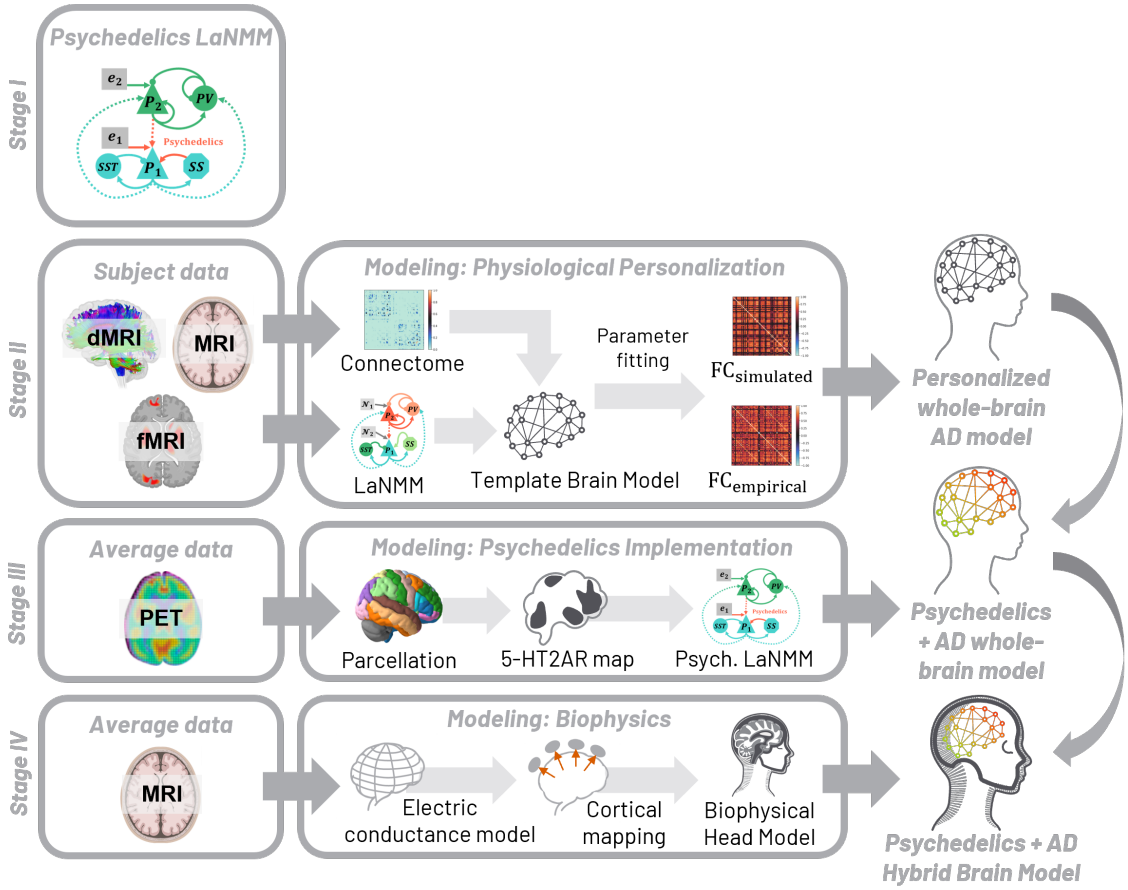

Figure 1: Overview of the methodology. — Pipeline for personalization of hybrid brain models of AD and the effects of psychedelics using structural MRI, dMRI, fMRI, and PET data.

oscillations in a cortical column.[53] The JR NMM model can generate slow oscillations in the alpha band (8–12 Hz) and is adjusted to oscillate at 10 Hz at baseline conditions. A variation of the PING model modified to oscillate at 40 Hz at baseline conditions produces fast oscillations in the gamma band (30-70 Hz).

The JR sub-circuit (Figure S1) consists of a population of pyramidal neurons (representing layer 5 pyramidal cells; P_1) coupled via excitatory connections to a population of excitatory neurons (representing mostly spiny stellate neurons; SS) and to a population of slow inhibitory interneurons (representing somatostatin-expressing cells; SST). Both SS and SST populations are reciprocally coupled to P_1 through excitatory and inhibitory synapses, respectively. On the other hand, the PING sub-circuit consists of a population of pyramidal cells (representing layer 2/3 pyramidal cells; P_2) and a population of fast inhibitory interneurons (representing parvalbumin-positive cells; PV). External perturbations e_1 and e_2 are applied to P_1 and P_2, respectively, to represent the influence of other brain areas. The PING and JR sub-circuits are reciprocally coupled through excitatory connections between the pyramidal populations P_1 and P_2 and through the PING's inhibitory population, thus constituting a single NMM. A schematic diagram can be found in Figure S1. The

equations and model parameters for the LaNMM have been presented in previous work[53] and are detailed in Supplement S.2 and Table S1.

The novelty of the present study resides in the implementation of psychedelic effects into NMMs (Stage I in Figure 1). The increased excitability to glutamate inputs observed under psychedelics can be translated into an increase of the average synaptic gain A_{L5P} parameter of excitatory connections to L5 pyramidal populations in the LaNMM. This parameter determines the extent to which the average firing rate of a population of neurons increases or decreases in response to an input membrane potential perturbation. Three glutamatergic connections to L5 pyramidal neurons are present in the LaNMM: connections from the SS and P_2 populations to P_1, and external noise perturbation e_1 to P_1 (connections 1, 11 and 3 in Figure S1). Hence, we model 5-HT2AR activation via serotonin neurotransmission by transforming receptor stimulation into changes of the excitatory synaptic gain A_{L5P} in those connections.

We first studied the dynamics of a single uncoupled LaNMM for different A_{L5P} values in the three targeted connections. For simplicity, we modified this parameter equally for all these synapses, assuming that the activation of 5-HT2ARs affects similarly all L5 pyramidal synapses in a particular cortical column. We have used the average membrane potential activity of the pyramidal populations to study the dynamics of the uncoupled LaNMM, given that pyramidal neurons are thought to be the main contributors to the potential recorded in electrophysiological signals such as EEG.[59,60]

The model was simulated for each gain value $A_{L5P} \in [0, 10]$ mV in increasing steps of 0.05 mV. In each simulation, A_{L5P} was simultaneously and equally increased in all three target connections and the LaNMM was run for a duration of 40 s with a sampling frequency $f_s = 1000$ Hz. Then, the PSD of the membrane potential of each pyramidal population P_1 and P_2 was computed for the last 30 s of the simulation to allow the model's convergence to the steady state. Throughout the study, the PSD is calculated using Welch's method[61] with a segment length $L = 1000$ samples.

2.2 Baseline AD whole-brain models

The next step in our study was to create personalized whole-brain models of AD subjects based on the LaNMM to later introduce the effects of psychedelics. In what follows, we summarize the methodology used to obtain such whole-brain models, illustrated in Figure 1 (stage II) and based on our previous work.[55,56]

Data acquisition

We used data of 30 AD subjects from the Alzheimer's Disease Neuroimaging Initiative 3 (ADNI3) database (https://adni.loni.usc.edu/). The ADNI was a multicenter study initiated by Michael W. Weiner in 2004 which focused on the early diagnosis and follow-up of AD. The cohort consisted of individuals diagnosed with AD (13 women), with a mean age of 73.6 years (SD: 7.32). The average Mini-Mental State Examination (MMSE) score, a standard measure of cognitive function,

ranged from 17 to 30 (mean: 22.5, SD: 2.7), reflecting variability in the extent of cognitive decline among the subjects selected.

The model personalization pipeline involves three types of neuroimaging data: MRI, dMRI, and blood-oxigen-level-dependent (BOLD) resting-state fMRI (rs-fMRI). T1-weighted MRI images were acquired using standardized MPRAGE protocols with 3T MRI scanners across multiple sites. Key acquisition parameters included TR = 2300 ms, TE = 2.98 ms, voxel size = 1×1×1 mm, and flip angle = 9°. Resting-state fMRI data were acquired using standardized ADNI3 protocols with gradient-echo EPI sequences. Key parameters included TR = 3000 ms, TE = 30 ms, flip angle = 90°, voxel size = 3.3×3.3×3.3 mm, and scan duration = ∼6 minutes. Diffusion MRI was acquired with b-values of 0 and 1000 s/mm^2, 41 gradient directions, TR = ∼9100 ms, TE = ∼98 ms, and voxel size = 2.7×2.7×2.7 mm. Detailed imaging protocols and scanner-specific adjustments are available in the ADNI3 documentation.

Data processing

Each modality underwent a dedicated processing pipeline to generate subject-specific inputs for the whole-brain models. T1-weighted MRI data was used to create a subject-specific Desikan-Killiany (DK-68) cortical atlas.[62] The MRI processing pipeline, based on FreeSurfer,[63] began with cortical reconstruction using the *recon-all* function to extract the pial surface. The DK68 parcellation, provided by FreeSurfer, was mapped to the subject-specific brain structure. This volumetric image served as the basis for processing dMRI and rs-fMRI data.

Diffusion MRI data was processed to calculate the subject's structural connectome (SC). Preprocessing steps included denoising, artifact correction (e.g., eddy currents), and estimating the fiber orientation density using constrained spherical deconvolution. Probabilistic tractography was then performed with MRtrix3,[64] generating 20 million streamlines constrained to start and terminate in gray matter parcels defined by the MRI parcellation. The resulting structural connectome matrix quantified the number of streamlines connecting each pair of parcels and was normalized by the total number of fibers and the number of parcels to generate a connectivity matrix for the subject.

BOLD rs-fMRI data was preprocessed using fMRIPrep 22.0.0,[65] which utilizes Nipype 1.8.3.[66] For anatomical data, T1-weighted images were corrected for intensity non-uniformity (N4BiasFieldCorrection) and skull-stripped using ANTs.[67] Tissue segmentation was performed with FSL FAST, and brain surfaces were reconstructed with FreeSurfer. Functional data preprocessing included motion correction (FSL mcflirt), slice-timing correction (AFNI 3dTshift), co-registration to T1-weighted images (FreeSurfer bbregister), and normalization to MNI templates using ANTs. Confound regressors, including motion parameters, CompCor components, and frame-wise displacement, were calculated to facilitate nuisance regression. Detailed preprocessing workflows and parameters are described in the supplementary materials and in the fMRIPrep documentation (https://fmriprep.org).

Model fitting

In our framework, whole-brain models represent the human cortex as a network of coupled NMMs, with each node representing the average activity of a cortical parcel through a LaNMM and each link between them modeling the white matter fibers connecting these parcels. The connectome (obtained from dMRI data as described above) was used to provide the connectivity between nodes. P_1 and P_2 populations of different parcels i, j were connected as follows: $P_1^i \rightarrow P_1^j$ (lateral connection), $P_1^i \rightarrow P_2^j$ (feedback or descending connection) and $P_2^i \rightarrow P_2^j$ (feedforward or ascending connection) with relative weights of 0.5, 0.5 and 1 respectively. Further details about the long-range connectivity are given in Appendix S.2.2.

Whole-brain models were personalized to match each subject's empirical functional connectivity (FC) obtained from their BOLD rs-fMRI, ultimately tailoring the models to reflect individual neural dynamics. Synthetic BOLD data from the whole-brain models was generated using the Balloon-Windkessel model,[68] and FC matrices were computed using Pearson's correlation coefficient (PCC) between the BOLD signals. Each whole-brain model was simulated for five different noise realizations for a duration of 300 s with a sampling frequency of $f_s = 1000$ Hz. The first 5 seconds of the simulation were discarded to account for transient dynamics and ensure the models reached a steady state. The RK4 method was used to solve the model's differential equations.

Model optimization involved tuning the global coupling gain G (which scales the connectome) and the noise received by the pyramidal populations of each region (in particular, the ratio between common and homotopic noise standard deviations (SDs) σ_c/σ_i, see Appendix S.2.3). A grid search was performed to select the optimal values of G and noise that minimized the root mean squared error (RMSE) between simulated and empirical FC matrices for each subject. The best value across noise realization was selected. An additional constraint was applied, requiring the PCC between simulated and empirical FC matrices to be higher than the PCC between the empirical FC and the structural connectivity matrix. This ensured that the models captured FC patterns beyond those explained by anatomical connectivity.

2.3 Whole-brain models under psychedelics

The 30 subject-specific whole-brain models described in Section 2.2 were adapted to reproduce the activation of 5-HT2A receptors (Stage III in Figure 1). Following our approach of implementing psychedelic effects into NMMs described in Section 2.1, we integrated 5-HT2A receptor data in the baseline-fitted whole-brain models to reproduce activation of these receptors by modulating the synaptic gain of all excitatory inputs to P_1 pyramidal population (A_{L5P}) in every LaNMM of the brain network. This includes connections from the SS and P_2 populations to P_1, the common and homotopic external inputs (see Appendix S.2.3), and all $P_1 \rightarrow P_1$ long-range cortico-cortical inputs.

To modulate the average synaptic gain of the connections involved in the psychedelic effect, we used 5-HT2A receptor density data informed by the high-resolution *in vivo*

atlas of the human brain serotonin system measured with PET in Beliveau et al.[69] We refer the reader to that paper for further details on the PET and MRI acquisition parameters and the participant's demographics. We parcellated the 5-HT2AR average density map into the DK-68 cortical atlas as detailed in Appendix S.3. We then normalized the density values B_{max} to fall between 0 and 1. This provides us with the relative spatial distribution of 5-HT2A receptors between brain areas, defining the amount of serotonergic stimulation each brain area experiences under psychedelic drugs.

To translate the receptor density map into average synaptic amplitude gain values of glutamatergic connections to P_1 (A_{L5P}), we define the neuromodulation relation

$$A^i_{L5P} = A_0 + \psi \cdot R_i \cdot (A_{\max} - A_0) \tag{1}$$

where ψ is the psychedelic dose (0 at baseline, 1 under psychedelics) and $R_i \in [0, 1]$ is the normalized parcel's receptor density. $A_0 = 3.25$ mV is the nominal gain, i.e., the average synaptic amplitude (PSP) gain of pyramidal neurons at baseline conditions.[50] $A_{\max} = 3.75$ mV is the maximum gain, i.e., the gain at which the PSD decay of the alpha band in the P_1 population ceases to be linear when increasing A_{L5P} in an uncoupled LaNMM, determined as explained in Section 3.1. Hence, this maps the receptor densities between A_0 and $A_{\max}$ and maintains a linear relationship between R and A_{L5P}. The normalization applied to B_{max} assumes that the minimum density of receptors corresponds to the nominal gain A_0. Of note, we use the same $A_{\max}$ value in all parcels and apply the same spatial distribution of 5-HT2AR densities to each subject.

To study the whole-brain effects of psychedelics, each subject's whole-brain model was simulated for a duration of 40 s with a sampling frequency $f_s = 1000$ Hz. The RK4 method was used to solve the model's differential equations. The first 10 seconds of the simulation were disregarded in all subsequent analyses to account for the transient time of the models and their convergence to the steady state.

2.4 Simulation of EEG recordings using hybrid brain models

We generated synthetic EEG data for each subject using hybrid brain models, which combine the physiological whole-brain models developed in the previous section with a biophysical head model template[70–72] (Stage IV in Figure 1). The process of EEG generation from the simulated activity in the whole-brain model NMMs can be divided into two steps: 1) generation of the equivalent dipole strength over time from NMM activity, 2) generation of EEG signals from the dipole strength.

To translate NMM activity into the equivalent dipole strength, we used the mesoscale physical model of volume conduction and the neuron compartment models of current generation from Mercadal et al. (2023),[57] which were developed based on the laminar framework developed in Sanchez-Todo et al. (2023).[53] In brief, a multicompartmental modeling formalism and detailed geometrical models of pyramidal cells are used to simulate the transmembrane currents due to synaptic inputs into different cortical layers. These results are linearly combined to estimate the total current source densities (CSDs) generated due to the neural activity in pyramidal

populations, which are considered the main current generators.[59,73] The CSDs are then used to calculate the equivalent dipole strength over time associated with the neural activity in each parcel of the subject-specific whole-brain model.

To generate scalp EEG signals from the dipole activity, we combined the personalized whole-brain model with a template biophysical head model, creating a hybrid brain model.[56] Appendix S.4 details the process of template head model creation. We used such a head model of electrical conduction to compute cortical mappers for EEG and generate the EEG signals in each electrode from the equivalent dipole strength computed in the personalized whole-brain models.

2.5 Complexity and entropy of simulated EEG

To capture the complexity of the simulated EEG signals obtained from the personalized whole-brain models under psychedelics, we used the notion of algorithmic complexity (or Kolmogorov complexity), which defines the length of the shortest program capable of generating a given string. Since algorithmic complexity is challenging to estimate directly, we use practical approximations based on measures of complexity derived from Lempel–Ziv compression and entropy rate, as detailed in Ruffini et al. (2019).[74,75]

We estimated the *Lempel-Ziv complexity* of the EEG data signals using the Lempel-Ziv-Welch (LZW) method.[74–77] We used a single 5-second epoch of simulated broadband EEG data (0.5–100 Hz) generated from each subject's personalized computational model for this calculation and the subsequent entropy rate analysis, as the intrasubject variability of the synthetic data was negligible. The 5-second epoch of each channel was binarized based on the median value of the epoch: each value was converted into a '0' if it was below the median and into a '1' otherwise.[74] The binarized data of all channels was concatenated and the LZW method was applied to the resulting string. A natural way to normalize the description length resulting from the LZW method, l_{LZW}, is to divide it by the original string length n, $\rho_0 = l_{LZW}/n$, with units of bits per character. We computed ρ_0 following this method for each subject.

To complement this analysis, we computed the related *entropy rate* of the binarized EEG signals for each subject. For a stationary stochastic process $\{X_i\}$, the entropy rate $\mathcal{H}(X)$ is defined as

$$\mathcal{H}(X) = \lim_{n\to\infty} \frac{H(X_1, \ldots, X_n)}{n} = \lim_{n\to\infty} H(X_n \mid X_{n-1}, \ldots, X_1),$$

where $H_n(X) = H(X_1, \ldots, X_n)$ is the joint entropy and $H(X) = -\mathbb{E}_X[\log P(X)]$. For a Markov process of order n, the entropy rate simplifies to the conditional entropy given the previous n states. In the special case of $n = 0$ (an independent and identically distributed process), the entropy rate reduces to the entropy of a single symbol, $H(X_i)$. Following these definitions, we computed the entropy rate for Markov orders $n = 0, \ldots, 5$.[75,76]

Finally, we calculated the *spectral entropy* of the 5-second epoch of simulated EEG as an alternative measure of neural entropy under baseline and psychedelic con-

ditions. To achieve this, for each subject, the PSD was averaged across channels and normalized to sum to 1, thereby transforming it into a probability distribution function (PDF). The spectral entropy was then computed for each channel using Shannon's entropy, $H(p) = -\sum p_i \cdot \log p_i$, where p_i is the PSD normalized to unit sum.

3 Results

3.1 Uncoupled LaNMM spectral profile

We first studied the power spectrum of pyramidal populations P_1 (generator of alpha oscillations) and P_2 (generator of gamma oscillations) in an uncoupled LaNMM, and assessed the LaNMM's ability to simulate the cortical spectral alterations resulting from 5-HT2AR psychedelics activation in this range.

Figure 2 shows the mean PSD in the alpha and gamma bands of populations P_1 and P_2 for different synaptic gains $A_{L5P} \in [0, 10]$ mV. We can observe a window of synaptic gain values $A_{L5P} \in [2.75, 4.15]$ mV for which both alpha and gamma oscillations are present in the LaNMM (as further detailed in Appendix S.5).

The results show a main peak in the mean PSD of P_1's alpha band coinciding with the start of the gamma oscillations in P_2 at $A_{L5P} = 2.75$ mV. The decay of alpha activity in P_1 starts concurrently with the growth of gamma activity in P_2, indicating a reciprocal and inverse relationship to synaptic gain changes between the two pyramidal populations for $A_{L5P} \in [2.75, 4.15]$ mV. The nominal synaptic gain $A_0 = 3.25$ mV used in Sanchez-Todo et al. (2023)[53] and Jansen and Rit (1995)[50] falls within this interval. This indicates that at baseline conditions (no psychedelics applied), P_1 oscillates in the alpha band and P_2 in the gamma band. The decay of alpha power in P_1 becomes nonlinear at around 3.75 mV, with a PSD in alpha of about 0.1 mV^2/Hz. We will use this value as the maximum gain of the pyramidal

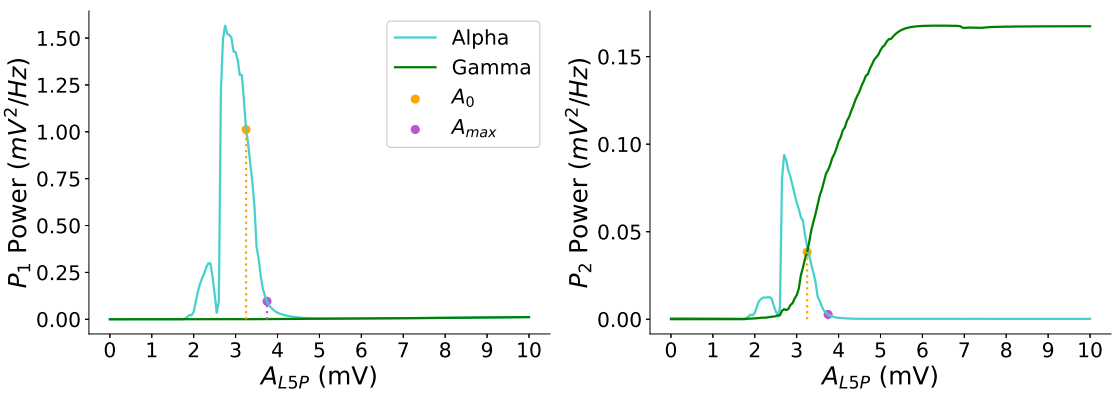

Figure 2: Uncoupled LaNMM spectral profile — Mean PSD of the membrane potential of P_1 (left) and P_2 (right) in the alpha band (blue) and gamma band (green) for different values of synaptic gain A_{L5P}. The vertical dashed lines indicate the nominal gain A_0 (orange) and the maximum gain $A_{\max}$ (purple), respectively.

populations in our model, $A_{\max} = 3.75$ mV (corresponding to a minimum PSD in the alpha band of $PSD^{\alpha}_{\min} = 0.1\text{mV}^2/\text{Hz}$).

These findings substantiate two key observations. First, the decrease in alpha power in P_1 and the increase in gamma power in P_2 can be reproduced in the model through the selective increase of glutamatergic gain of synapses targeting L5 pyramidal neurons, associated with higher 5-HT2AR densities. This agrees with previous empirical observations found in the literature.[1,8,16–18] Second, the inverse relationship between alpha and gamma power is sustained within our regime of interest $A_{L5P} \in [A_0, A_{\max}]$. It is worth mentioning that the most significant changes induced by psychedelics in the PSD magnitude in our LaNMM are specific to the alpha and gamma bands within the gain range under study $[A_0, A_{\max}]$ in both P_1 and P_2 populations (Figure S6).

3.2 Whole-brain model personalization

After studying the uncoupled laminar model, we now study the model at the whole-brain level. We created personalized whole-brain models for 30 AD subjects. The personalization resulted in high similarity between the subjects' rs-fMRI BOLD FC and the synthetic FC obtained with the fitted model, with an average PCC across subjects of 0.45 and an average RMSE of 0.18 after model personalization.

For all subjects, we found higher similarity (captured with RMSE and PCC) of the empirical FC with the model-generated FC than with the structural connectivity, confirming that the models were able to explain the functional data beyond the information provided by the subject-specific connectome alone (Figure 3a). The values of PCC, RMSE, and fitted parameters for each subject can be found in Supplementary S.6, as well as the empirical and synthetic FC matrices for each subject.

As an example of model parameter optimization, Figure 3b shows the grid search performed to find the minimum value of RMSE for different combinations of G and σ_c/σ_i for one subject model personalization. The FC matrices obtained from the synthetic BOLD signal for the optimal parameter selection for this subject are shown in Figure 3c and compared with the subject's BOLD FC, showing the similarity between both matrices.

We then analyzed the optimal G parameter values found for each subject and their relationship to the alpha activity at baseline, which is crucial for the simulation of the effects of psychedelics in the model. Figure 3d shows the G parameter across subject models and the percentage of parcels in each model that are above the threshold of mean PSD for P_1's alpha band (i.e, $PSD^{\alpha}_{P_1} > PSD^{\alpha}_{\min}$). We ordered the values according to the magnitude of the personalized G parameter to facilitate the visualization. The high negative correlation observed between alpha activity and G ($r_{PCC} = -0.80,\ p < 0.0001$) evidences that personalized models with higher G values have less overall alpha activity in the brain. Since G controls the global excitation of the brain model, the higher G is, the more the P_1 population activity approaches the region where alpha activity is lost (see Figure S5).

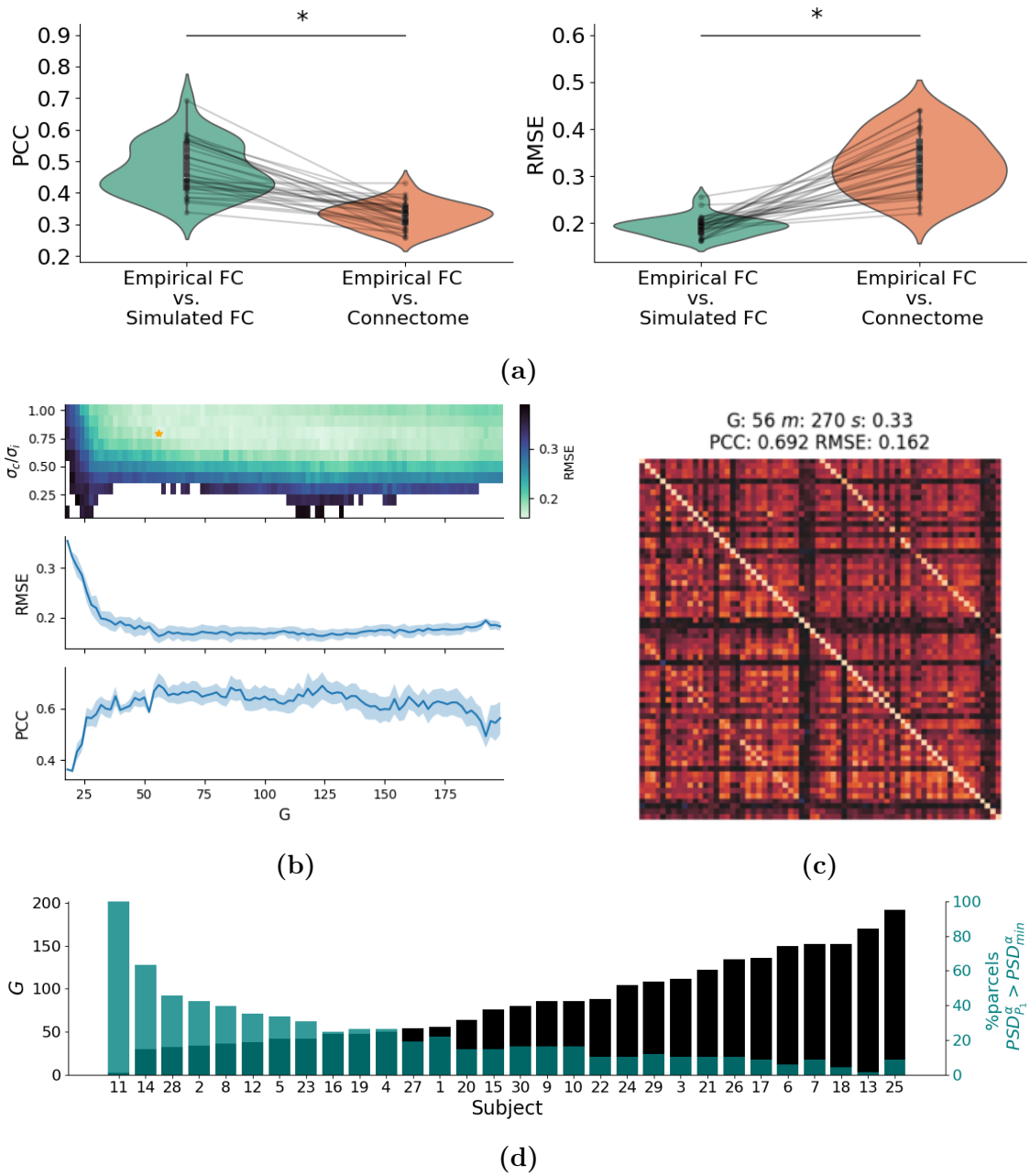

Figure 3: Whole-brain model fitting results (a) PCC and RMSE between the empirical FC and simulated FC compared with the PCC and RMSE of the empirical FC and the structural connectome. **(b)** Example of model personalization (subject 1): RMSE between empirical and synthetic FC for different values of the parameters G and σ_c/σ_i (top), RMSE and PCC as a function of the G value (center and bottom). **(c)** For the same subject, comparison between the empirical rs-fMRI BOLD FC (lower triangular matrix) and the synthetic FC obtained with the fitted model (upper triangular matrix). **(d)** Optimal G parameter found for each subject-specific model (from lowest to highest) and number of DK-68 parcels of each model with meaningful alpha activity in P_1 ($PSD^{\alpha}_{P_1} > PSD^{\alpha}_{\min}$).

Of note, subject 11 showed an abnormally low G, which results in alpha oscillations in all cortical areas due to a globally diminished excitability. Upon deeper inspection, we noted that for this subject the grid-search selected parameter values resulted in total disconnection between nodes, leading to non-realistic dynamics. On the other hand, subject 13 shows an abnormally low alpha activity at baseline with only one alpha-active parcel, which is strongly related to its high G value. Further analysis revealed that all subjects except for subject 13 were responsive to 5-HT2AR stimulation. For these reasons, we excluded both subjects 11 and 13 from the calculations and analysis in the next sections.

It is worth mentioning that, on average, only 21% of the parcels have meaningful alpha activity at baseline (that is, above $PSD^{\alpha}_{\text{min}}$) in the personalized models. Nevertheless, the models are able to reproduce significant changes in the mean alpha band activity following the simulation of 5-HT2AR activation, as shown in the next section.

3.3 Whole-brain spectral profile under psychedelics

Next, we studied the power spectrum of the AD whole-brain models and the spectral changes caused by psychedelics at the brain network level. We computed the parcel-averaged power spectrum of each subject's membrane potential and conducted Wilcoxon signed-rank tests in each brain band (delta: 0.5–4 Hz, theta: 4–8 Hz, alpha: 8–12 Hz, beta: 12–30 Hz, and gamma: 30-70 Hz), comparing the mean PSD in each frequency band across subjects between the baseline and psychedelic conditions. We used the Wilcoxon signed-rank test as a non-parametric alternative to the paired t-test, given that the data did not conform to a normal distribution according to the Kolmogorov–Smirnov test (Bonferroni-corrected $p<0.05$ in all frequency bands and conditions).

Figure 4 displays the power spectrum in P_1 and P_2 averaged across parcels and subjects and the results of the Wilcoxon signed-rank test. Consistent with our findings for the uncoupled LaNMM, clear peaks are observed in the alpha and gamma bands in the baseline condition. Moreover, the statistical analyses revealed a significant decrease in mean alpha power in both P_1 (-61%) and P_2 (-44%) and a significant increase in mean gamma power in both P_1 (-25%) and P_2 (-3.5%). The level of significance across tests was Bonferroni-corrected. The tendency towards a decrease of alpha power and an increase of gamma power in both pyramidal populations was consistently observed in all subjects, as shown in Figure 4b.

Although our model was specifically designed to produce alpha and gamma oscillations, we observed significant alterations across all bands and pyramidal populations under psychedelic conditions. Alpha and beta oscillations decreased on average with 5-HT2AR stimulation, while gamma oscillations increased. Nevertheless, the delta and theta bands showed discrepancies between the two pyramidal populations since their mean power consistently increased in P_1 but decreased in P_2 in every subject. The large standard deviation seen for the alpha band is consistent with the high variability seen in alpha power and G values between different subjects in Figure 3d.

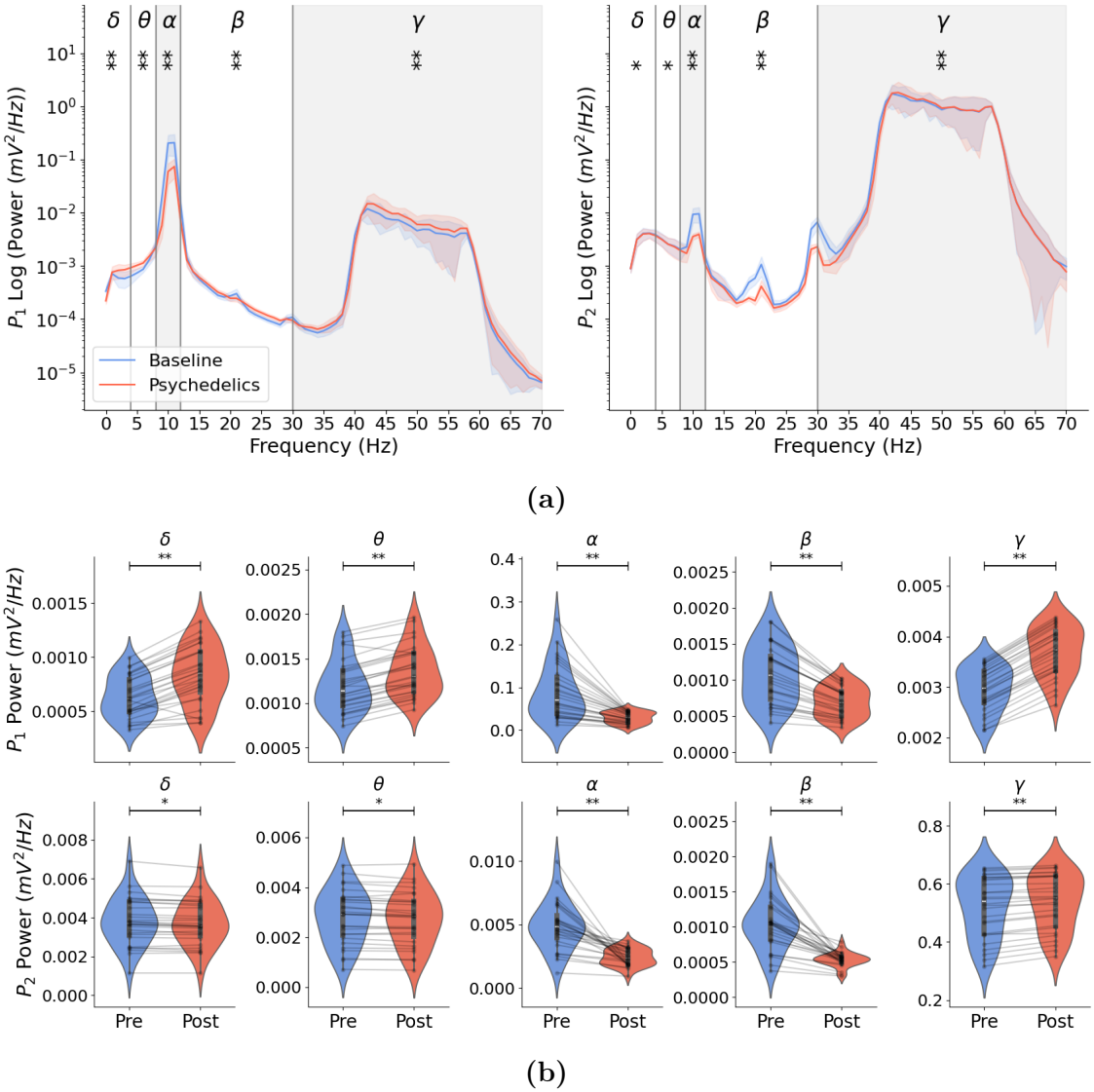

Figure 4: Whole-brain models reproduce the power spectrum alterations associated with psychedelics — **(a)** Power spectrum of P_1 (left) and P_2 (right) membrane potential averaged across brain parcels and subjects. Shaded areas represent the median absolute deviation across subjects, and solid line curves represent the average across subjects. The significance level (Bonferroni-corrected) of the average PSD difference between conditions in each band is denoted by the number of asterisks (*p $<$ 0.05, **p $<$ 0.0001). **(b)** Parcel-averaged membrane potential PSD of P_1 (top) and P_2 (bottom) in different bands across subjects. Black bars represent the interquartile range, and a central white dot indicates the median PSD. Individual dots connected by grey lines represent the mean power for each subject. Asterisks denote statistical significance as described above.

Alterations in the beta band result from the harmonics of alpha oscillations (see Figure S6), while changes in the theta and delta frequency bands mainly result from the external noisy input introduced to population P_1, a connection also susceptible to 5-HT2AR stimulation. The frequency power analysis also highlights that the

greatest magnitude change in PSD is specific to the alpha and gamma frequency bands, which are the main focus of our study.

3.4 Influence of 5-HT2AR distribution on oscillatory activity

The changes in the spatial distribution of alpha and gamma activity across the brain are expected to relate to the applied PET-informed distribution of neurotransmitter densities. To evaluate this, we measured the PCC between the parcels' density of 5-HT2A receptors and their absolute PSD difference ($PSD_{\text{Post}} - PSD_{\text{Pre}}$) in both the alpha and gamma bands. Parcels with $PSD^{\alpha}_{P_1} < PSD^{\alpha}_{\text{min}}$ at baseline were excluded from the analysis since their alpha power was not expected to show relevant variations due to changes in receptor density.

Figure 5 shows the results of the analysis averaged across subjects (i.e., PSD difference of the parcel averaged across subjects). We found strong correlations for both the alpha band (P_1 $r_{\text{PCC}} = -0.38, p < 0.009$) and the gamma band ($P_1$ $r_{\text{PCC}} = 0.91, p < 0.0001$; P_2 $r_{\text{PCC}} = 0.49, p < 0.0001$), except for the alpha power in P_2 ($r_{\text{PCC}} = -0.04, p = 0.7$). This suggests that regions with the highest expression of 5-HT2A receptors were most affected by psychedelics in the model. Hence, the power spectrum changes in our models are mainly explained by the applied spatial distribution of 5-HT2A receptors.

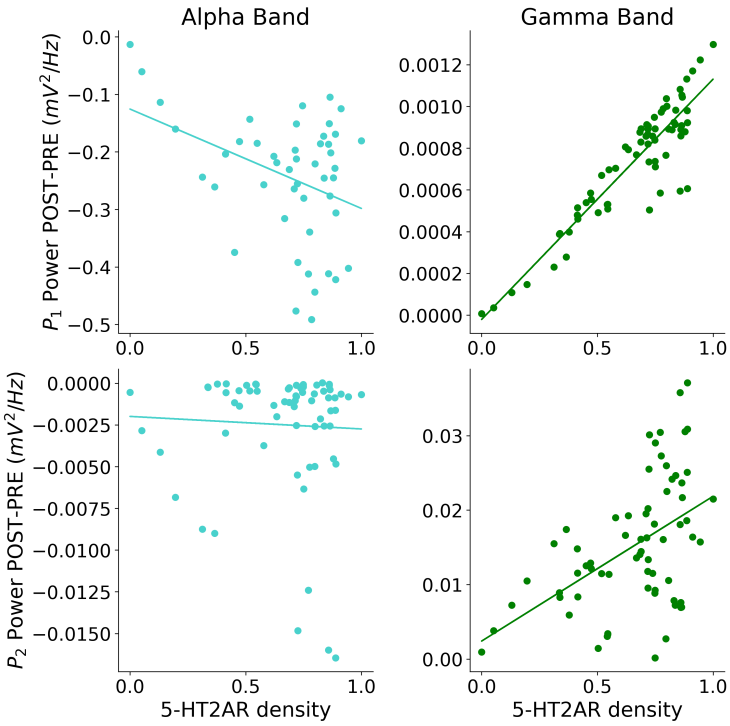

Figure 5: Spectral alterations under psychedelics reflect the spatial distribution and density of 5-HT2A receptors — Subject averaged parcel alpha band (left) and gamma band (right) membrane potential PSD difference ($PSD_{\text{Post}} - PSD_{\text{Pre}}$) against parcel 5-HT2AR density in P_1 (top) and P_2 (bottom). Each dot represents a parcel, solid lines showing linear regression fits.

3.5 Model-generated EEG alpha and gamma power

Finally, we studied the power spectrum alterations induced by psychedelics in EEG data. We computed the power spectrum of each EEG channel averaged across subjects. Figure 6a shows the subject-averaged topographic map of the power in the alpha and gamma bands computed from the simulated EEG signals in the AD whole-brain models with and without psychedelics. We then conducted Wilcoxon signed-rank tests in the alpha and gamma bands comparing the mean band PSD of both conditions. The use of the Wilcoxon signed-rank test was again justified by the non-normal distribution of the data, confirmed by the Kolmogorov-Smirnov test (Bonferroni-corrected $p<0.05$ in all EEG channels and conditions). Figure 6b shows the subject-averaged PSD difference between the baseline and psychedelic conditions, along with the statistical significance of the changes in each EEG electrode given by the analysis described above.

Consistent with our previous results, the EEG shows a brain-wide decrease of alpha power in the spontaneous brain activity of all the modeled subjects (62% mean alpha PSD decrease with respect to baseline averaged over subjects and EEG channels). This decrease is significant across all EEG channels, and highly significant decreases

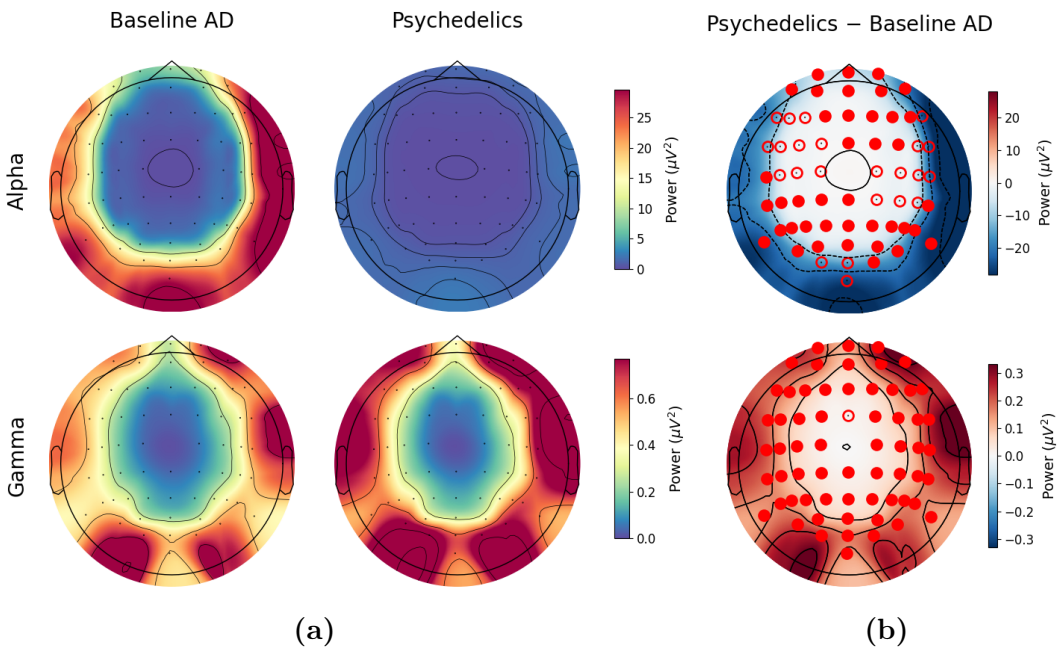

Figure 6: Model reproduces EEG alpha and gamma changes following 5-HT2AR stimulation with psychedelics — **(a)** Subject-averaged topographic map of the mean alpha and gamma band's EEG PSD for the AD whole-brain models with and without stimulation by psychedelics. Black dots denote the recording location of the EEG electrodes. **(b)** Subject-averaged EEG PSD difference between the baseline AD models and the models with psychedelics effects (psychedelics − baseline). The statistical significance (Bonferroni-corrected) of the PSD changes in each EEG channel is denoted by an empty red dot ($p < 0.05$) or a filled red dot ($p < 0.001$) on top of the corresponding electrode.

in alpha power ($p < 0.001$) were consistently observed in all subjects and in all brain lobes. On the other hand, we found a significant increase in the EEG gamma band power after 5-HT2AR stimulation (37% mean gamma PSD increase with respect to baseline averaged over subjects and EEG channels). This increase is significant across all EEG channels and was consistently observed in all subjects.

It is worth mentioning that the cortical distribution of alpha and gamma activity in the synthetic EEG may not fully align with the spectral features typically observed in the EEG of healthy or AD individuals. The reduced oscillatory activity in both alpha and gamma frequencies in the parietal regions may be explained by the fact that the whole-brain models developed in this study were not personalized based on EEG data but on fMRI data. Inspection of the connectivity matrix revealed that this reduced EEG power can be mostly explained by a saturation of the connections to the parietal lobe. Indeed, the parietal lobe acts as a network hub, and the neural populations in this lobe receive high inputs and consequently often show saturated activity in the model. This hinders the emergence of oscillatory activity in alpha and gamma frequencies, resulting in the decreased alpha and gamma power observed in the parietal and parieto-frontal areas.

3.6 Simulated EEG complexity and entropy

Next, we used different metrics to capture the complexity of the simulated EEG signals obtained from the personalized hybrid brain models under psychedelics. Given the non-linear dynamics of EEG signals, we selected metrics that estimate upper bounds on algorithmic complexity (see Section 2.5). The normalized LZW complexity (ρ_0) of EEG signals in subjects under psychedelics was significantly higher than at baseline (Figure 7, left), demonstrating that the oscillatory changes induced by psychedelics in the whole-brain models lead to increased complexity of the signals.

This was further highlighted by the significant increase in spectral entropy (Figure 7, middle) and entropy rate at different Markov orders (Figure 7, right). The normalized LZW complexity reflects the structural richness of the signal, while the spectral entropy indicates a more uniform power distribution across frequencies, consistent with increased neural variability mainly explained by the decreased power in the alpha band (Figure 4b). The entropy rate at different orders provides a measure of the temporal predictability of the EEG signals, highlighting how psychedelics induce more diverse oscillatory patterns in the models.

4 Discussion

4.1 Main findings

Our modeling implementation of psychedelics' effects into NMMs successfully explains the power spectrum typically observed after administration of psychedelics in all the modeled subjects and is consistent with the results documented in the experimental literature.[8,16–18]

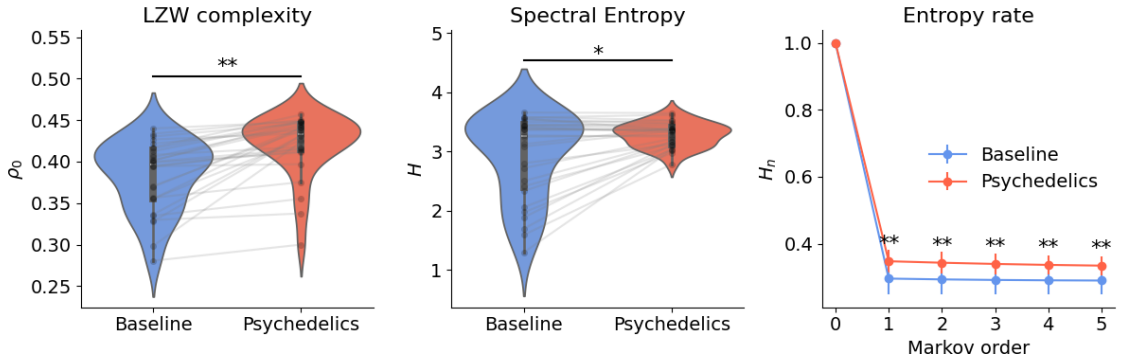

Figure 7: Model reproduces complexity and entropy changes under psychedelics — Left: Normalized LZW complexity of broadband EEG for the whole-brain models at baseline and under psychedelics. Black bars represent the interquartile range, and a central white dot indicates the median complexity. Individual dots connected by grey lines represent the signal complexity for each subject. **Middle:** Spectral entropy of broadband EEG signals for both conditions. **Right:** Entropy rate for different Markov orders of broadband EEG signals in the baseline and psychedelics conditions. Error bars indicate the standard deviation across subjects. In all cases, the significance level of the difference between conditions resulting from a paired t-test (Bonferroni-corrected for the entropy rate) is denoted by the number of asterisks (*p $<$ 0.001, **p $<$ 0.0001).

Previous empirical studies have observed multiband alterations in EEG data of healthy individuals under different psychedelic drugs.[17,18] Although a decrease in alpha activity and an increase in gamma have been consistently observed in EEG, the alterations in other frequency bands suffer variability among studies and measurement techniques. Timmermann et al. (2023)[18] recently performed a human neuroimaging study combining fMRI and EEG and offering a comprehensive view of the acute brain action of N,N-Dimethyltryptamine (DMT), finding a significant decrease in mean alpha and beta band power, together with a significant increase in mean gamma power. These results closely align with the findings obtained in the present study. The study of Ort et al. (2023)[17] showed similar results, revealing that mean theta and alpha power were significantly decreased in spontaneous EEG PSD under psilocybin. However, no significant changes were observed in other frequency bands.

We found a strong correlation between the changes in mean alpha and gamma power across the brain and the density of 5-HT2ARs in each brain area. Consequently, and consistent with our initial hypothesis, the significantly reduced alpha power and increased gamma power observed under the influence of psychedelics are mainly explained in our modeling framework by the agonism of these drugs on 5-HT2A receptors and the magnitude and spatial distribution of their effects are directly related to the expression amounts of such serotonin receptors.

Our findings align with experimental evidence linking psychedelics to enhanced neural entropy and complexity,[8,16,32] and support the potential therapeutic role

of psychedelics in restoring the complexity deficits observed in AD.[28,29] Different metrics of complexity and entropy (LZW, spectral entropy, and entropy rate) resulted in increased signal diversity and richness in the personalized models under psychedelics with respect to baseline. The ability of our whole-brain models to reproduce these effects highlights their utility in exploring the neural mechanisms underlying psychedelic-induced changes and their potential for counteracting pathological states associated with reduced complexity.

4.2 Potential therapeutic role of psychedelics in AD

Our results suggest that psychedelics may acutely mitigate EEG spectral alterations characteristic of AD, reinforcing their therapeutic potential for this neurodegenerative condition. The spectral shifts induced by psychedelics in our models may counteract the disrupted alpha-gamma coupling and oscillatory imbalances observed in AD induced by PV dysfunction, potentially improving functional connectivity and cognition. These results indicate that psychedelics may hold therapeutic potential in the AD stages characterized by alpha power increases and reduced gamma power (prodromal and mild AD).

However, we caution that in the preclinical and very early stages of AD, cortical neurons in certain regions exhibit heightened excitability, driven partly by elevated concentrations of soluble amyloid-beta, which impairs glutamate uptake and increases extracellular glutamate levels.[78–80] As activation of 5-HT2ARs by psychedelics modulates glutamate's excitatory effects, increasing the excitability of deep-layer pyramidal neurons,[15] their use under these conditions may intensify the existing hyperexcitability and accelerate pathological processes, suggesting a contraindication of such compounds during the earliest phases of AD. On the other hand, in the later stages of AD, the widespread loss of alpha and gamma power resulting from global neuronal death may render psychedelics ineffective as a treatment. This suggests there may be an optimal window for the treatment of AD with psychedelics, namely the prodromal to mild phase.

Importantly, the effects of psychedelics are not limited to their acute phase. Growing evidence highlights a post-acute phase characterized by enhanced neural plasticity, which underpins their long-term therapeutic effects.[81] This phase involves structural and functional neural changes that can promote sustained recovery of cognitive and neural functions, which is particularly relevant for addressing the progressive degeneration seen in AD. Thus, by recalibrating neuronal excitability and oscillatory activity, psychedelics may not only acutely alleviate acute EEG abnormalities but also facilitate long-term neural reorganization and plasticity. This aligns with prior research emphasizing the role of enhanced brain functional connectivity and neuroplasticity in slowing or reversing neurodegeneration.[4,5]

Finally, there is a natural synergy between psychedelics and non-invasive interventions such as transcranial electrical stimulation[82,83] or sensory stimulation,[84–87] which seek to entrain natural fast frequency circuits in AD. The combination of psychedelics with such interventions can produce benefits from the acute effects of each and by the increased window of plasticity facilitated by psychedelics.[81,88]

4.3 Limitations and future work

Several limitations in the present study are worth pointing out. Although our focus is on AD, the inclusion of data from healthy subjects could offer a critical comparative framework. By contrasting the altered alpha and gamma power in AD models treated with psychedelics against the normative power spectrum dynamics observed in healthy individuals, we might better understand the restorative potential of psychedelics. Such comparisons could elucidate whether the modeled oscillatory dynamics approximate—or fully restore—the canonical signatures of healthy brain activity.

Further validation of the proposed modeling framework might be achieved by including BOLD-fMRI data from healthy subjects under psychedelics. Specifically, this could be achieved by comparing the simulated FC with the empirical FC observed in individuals under psychedelics. Moreover, a multimodal approach —including concurrent EEG, could enhance validation. While our models were personalized using fMRI data, they did not include EEG data, which may explain the abnormally reduced alpha and gamma power observed in parietal areas. As a result, these models are not expected to accurately replicate the spatial distribution of oscillatory activity in the cortex. Future studies could address this by including EEG data from healthy subjects in the model optimization process to improve spatial accuracy.

Our AD model represents pathology only at the level of global connectivity and external noise. In parallel work in mesoscale modeling of AD, we have developed an adapted version of the LaNMM that reproduces the impact of PV synapse damage in oscillatory dynamics, producing slowing of EEG, increased alpha power, and reduced gamma.[54] In future work, we can investigate the effects of psychedelics in this AD mesoscale model, which incorporates physiologically-inspired mechanisms to reproduce the disruptions in oscillatory activity observed in AD.

The potential for lasting effects of psychedelics in AD assumes an "imprint model" of plasticity. This model assumes that when perturbations are applied to the brain (i.e., stimulation, psychedelics), they might induce transient changes in neural dynamics by modulating neuronal excitability and network oscillations. Hebbian plasticity mechanisms subsequently act on these perturbed dynamics, adjusting synaptic weights to reinforce connectivity patterns that facilitate the recurrence of the stimulated activity. This process creates a "plasticity imprint," effectively rewiring the network to make the occurrence of the perturbed dynamics more likely. Incorporating plasticity mechanisms into our models (e.g., Hebbian) would be crucial to further understand whether the new oscillatory regimes induced by psychedelics are indeed maintained over time and could contribute to sustained therapeutic benefits.

5 Conclusions

In this study, we explored the mechanisms behind spectral power alterations during the acute phase of serotonergic psychedelic drug effects and provided a novel mechanistic understanding of their impact on brain oscillatory dynamics. By implementing 5-HT2A receptor activation in a laminar neural mass model, we reproduced the char-

acteristic EEG multiband power spectrum alterations observed under psychedelics within a single cortical column. Extending this approach, we used 30 subject-specific whole-brain models, integrating MRI, dMRI, and fMRI data from AD subjects, to simulate the effects of psychedelics on whole-brain dynamics following 5-HT2A receptor stimulation.

The subject-specific whole-brain models effectively reproduced the power spectrum changes observed experimentally with psychedelics, notably the significant decreases in alpha and beta power and increases in gamma power. Our findings align with previous studies combining fMRI and EEG approaches to psychedelics[17,18] and further demonstrate a strong correlation between modulation of mean alpha and gamma power across brain regions and the spatial distribution of 5-HT2A receptors. By combining these whole-brain models with a biophysical head model, we successfully reproduced the suppression of alpha rhythms and increased gamma power observed in prior EEG studies as well as the complexity changes associated with the effects of psychedelics.

This modeling framework offers new insights into the neural mechanisms underlying psychedelic action and highlights the potential of psychedelics to restore healthy oscillatory dynamics in disorders like AD. Our approach paves the way for using computational whole-brain models to investigate the potential of psychedelics in rebalancing neural activity in neurodegenerative and psychiatric disorders.

Acknowledgements

We would like to thank the Elite Master Program in Neuroengineering at the Technical University of Munich, funded by the Elite Network of Bavaria, for the financial support.

Funding

Giulio Ruffini, Edmundo Lopez-Sola, Francesca Castaldo, Roser Sanchez-Todo, Èlia Lleal-Custey, and Ricardo Salvador are funded by the European Commission under European Union's Horizon 2020 research and innovation programme Grant Number 101017716 (Neurotwin) and European Research Council (ERC Synergy Galvani) under the European Union's Horizon 2020 research and innovation program Grant Number 855109. Jakub Vohryzek is funded by Neurotwin (855109). Jan C. Gendra is funded by the Elite Master Program in Neuroengineering at the Technical University of Munich, funded by the Elite Network of Bavaria. R.G.A acknowledges funding from the Spanish Ministry of Science and Innovation and the State Research Agency (Grant No. PID2020-118196GBI00/MICIU/AEI/10.13039/501100011033). Data collection and sharing for the Alzheimer's Disease Neuroimaging Initiative (ADNI) is funded by the National Institute on Aging (National Institutes of Health Grant U19AG024904). The grantee organization is the Northern California Institute for Research and Education.

Contributions

JCG: Conceptualization, Funding acquisition, Methodology, Software, Formal analysis, Investigation, Visualization, Writing – Original Draft, Writing – Review & Editing; EL-S: Conceptualization, Formal analysis, Methodology, Software, Visualization, Writing – Review & Editing; FC: Conceptualization, Writing – Review & Editing; EL-C: Methodology, Software, Writing – Review & Editing; RS-T: Conceptualization, Visualization, Writing – Review & Editing; RS: Methodology, Software, Writing – Review & Editing; JV: Conceptualization, Writing – Review & Editing; RGA: Conceptualization, Writing – Review & Editing; GR: Conceptualization, Funding acquisition, Methodology, Software, Writing – Original Draft, Review & Editing.

References

[1] Nutt D., Erritzoe D., and Carhart-Harris R. Psychedelic psychiatry's brave new world. *Cell*, 181(1):24–29, 2020.

[2] Husain M. I., Ledwos N., Fellows E., Baer J., Rosenblat J. D., Blumberger D. M., Mulsant B. H., and Castle D. J. Serotonergic psychedelics for depression: What do we know about neurobiological mechanisms of action? *Frontiers Psychiatry*, 13:1076459, 2023.

[3] Cameron L. P. and Patel S. D. et al. 5-ht2ars mediate therapeutic behavioral effects of psychedelic tryptamines. *ACS Chem Neurosci*, 14(3):351–358, 2023.

[4] Michael James Winkelman, Attila Szabo, and Ede Frecska. The potential of psychedelics for the treatment of Alzheimer's disease and related dementias. *European Neuropsychopharmacology: The Journal of the European College of Neuropsychopharmacology*, 76:3–16, November 2023.

[5] Albert Garcia-Romeu, Sean Darcy, Hillary Jackson, Toni White, and Paul Rosenberg. Psychedelics as Novel Therapeutics in Alzheimer's Disease: Rationale and Potential Mechanisms. *Current Topics in Behavioral Neurosciences*, 56:287–317, 2022.

[6] Simon Andrew Vann Jones and Allison O'Kelly. Psychedelics as a Treatment for Alzheimer's Disease Dementia. *Frontiers in Synaptic Neuroscience*, 12:34, 2020.

[7] Urszula Kozlowska, Charles Nichols, Kalina Wiatr, and Maciej Figiel. From psychiatry to neurology: Psychedelics as prospective therapeutics for neurodegenerative disorders. *Journal of Neurochemistry*, 162(1):89–108, 2022.

[8] Carhart-Harris R. L. and Friston K. J. Rebus and the anarchic brain: Toward a unified model of the brain action of psychedelics. *Pharmacol Rev*, 71(3):316–344, 2019.

[9] Carhart-Harris R. L. and Chandaria S. et al. Canalization and plasticity in psychopathology. *Neuropharmacology*, 226:109398, 2023.

[10] Warren A. L., Lankri D., Cunningham M. J., Serrano I. C., Parise L. F., Kruegel A. C., Duggan P., Zilberg G., Capper M. J., Havel V., et al. Structural pharmacology and therapeutic potential of 5-methoxytryptamines. *Nature*, pages 1–10, 2024.

[11] Hansen J. Y., Shafiei G., Markello R. D., Smart K., Cox S. M. L., Nørgaard M., Beliveau V., Wu Y., Gallezot J., Aumont É., et al. Mapping neurotransmitter systems to the structural and functional organization of the human neocortex. *Nature neuroscience*, 25(11):1569–1581, 2022.

[12] Madsen M. k., Fisher P. M., Burmester D., Dyssegaard A., Stenbæk D. S., Kristiansen S., Johansen S. S., Lehel S., Linnet K., Svarer C., et al. Psychedelic effects of psilocybin correlate with serotonin 2a receptor occupancy and plasma psilocin levels. *Neuropsychopharmacology*, 44(7):1328–1334, 2019.

[13] Luppi A. I., Girn M., Rosas F. E., Timmermann C., Roseman L., Erritzoe D., Nutt D. J., Stamatakis E. A., Spreng R. N., Xing L., et al. A role for the serotonin 2a receptor in the expansion and functioning of human transmodal cortex. *Brain*, 147(1):56–80, 2024.

[14] Berger M., Gray J. A., and Roth B. L. The expanded biology of serotonin. *Annu Rev Med*, 60:355–366, 2009.

[15] Andrade R. Serotonergic regulation of neuronal excitability in the prefrontal cortex. *Neuropharmacology*, 61(3):382–386, 2011.

[16] Carhart-Harris R. L. and Leech R. et al. The entropic brain: a theory of conscious states informed by neuroimaging research with psychedelic drugs. *Frontiers Human Neuroscience*, 8:20, 2014.

[17] Ort A. and Smallridge J. W. et al. Tms-eeg and resting-state eeg applied to altered states of consciousness: oscillations, complexity, and phenomenology. *iScience*, 26(5):106589, 2023.

[18] Timmermann C. and Roseman L. et al. Human brain effects of dmt assessed via eeg-fmri. *Proc Natl Acad Sci USA*, 120(13):e2218949120, 2023.

[19] Rebecca Smausz, Joanna Neill, and John Gigg. Neural mechanisms underlying psilocybin's therapeutic potential – the need for preclinical in vivo electrophysiology. *Journal of Psychopharmacology*, 36(7):781–793, July 2022.

[20] Akinori Nakamura, Pablo Cuesta, Alberto Fernández, Yutaka Arahata, Kaori Iwata, Izumi Kuratsubo, Masahiko Bundo, Hideyuki Hattori, Takashi Sakurai, Koji Fukuda, Yukihiko Washimi, Hidetoshi Endo, Akinori Takeda, Kersten Diers, Ricardo Bajo, Fernando Maestú, Kengo Ito, and Takashi Kato. Electromagnetic signatures of the preclinical and prodromal stages of Alzheimer's disease. *Brain: A Journal of Neurology*, 141(5):1470–1485, May 2018.

[21] Jonathan Gallego-Rudolf, Alex I. Wiesman, Alexa Pichet Binette, Sylvia Villeneuve, and Sylvain Baillet. Synergistic association of Aβ and tau pathology with cortical neurophysiology and cognitive decline in asymptomatic older adults. *Nature Neuroscience*, 27(11):2130–2137, November 2024.

[22] Sinead Gaubert, Federico Raimondo, Marion Houot, Marie-Constance Corsi, Lionel Naccache, Jacobo Diego Sitt, Bertrand Hermann, Delphine Oudiette, Geoffroy Gagliardi, Marie-Odile Habert, Bruno Dubois, Fabrizio De Vico Fallani, Hovagim Bakardjian, Stéphane Epelbaum, and Alzheimer's Disease Neuroimaging Initiative. EEG evidence of compensatory mechanisms in preclinical Alzheimer's disease. *Brain*, 142(7):2096–2112, July 2019.

[23] Roger Rochart, Quanying Liu, Alfred N Fonteh, Michael G Harrington, and Xianghong Arakaki. Compromised behavior and gamma power during working memory in cognitively healthy individuals with abnormal csf amyloid/tau. *Frontiers in Aging Neuroscience*, 12:574214, 2020.

[24] Dinavahi VPS Murty, Keerthana Manikandan, Wupadrasta Santosh Kumar, Ranjini Garani Ramesh, Simran Purokayastha, Bhargavi Nagendra, Abhishek

ML, Aditi Balakrishnan, Mahendra Javali, Naren Prahalada Rao, and Supratim Ray. Stimulus-induced gamma rhythms are weaker in human elderly with mild cognitive impairment and Alzheimer's disease. *eLife*, 10:e61666, June 2021. Publisher: eLife Sciences Publications, Ltd.

[25] Jorge J. Palop and Lennart Mucke. Network abnormalities and interneuron dysfunction in Alzheimer disease. *Nature Reviews. Neuroscience*, 17(12):777–792, December 2016.

[26] Chowtapalle Anuraag Chetty, Harsha Bhardwaj, G. Pradeep Kumar, T. Devanand, C. S. Aswin Sekhar, Tuba Aktürk, Ilayda Kiyi, Görsev Yener, Bahar Güntekin, Justin Joseph, and Chinnakkaruppan Adaikkan. EEG biomarkers in Alzheimer's and prodromal Alzheimer's: A comprehensive analysis of spectral and connectivity features. *Alzheimer's Research & Therapy*, 16(1):236, October 2024.

[27] Pilar Garcés, Raul Vicente, Michael Wibral, Jose Angel Pineda Pardo, Maria Eugenia Lopez, Sara Aurtenetxe, Alberto Marcos, Maria Emiliana de Andrés, Miguel Yus, Miguel Sancho, Fernando Maestú, and Alberto Fernández. Brain-wide slowing of spontaneous alpha rhythms in mild cognitive impairment. *Frontiers in Aging Neuroscience*, 5, December 2013.

[28] D. Abásolo, R. Hornero, P. Espino, D. Alvarez, and J. Poza. Entropy analysis of the EEG background activity in Alzheimer's disease patients. *Physiological Measurement*, 27(3):241–253, March 2006.

[29] Jie Sun, Bin Wang, Yan Niu, Yuan Tan, Chanjuan Fan, Nan Zhang, Jiayue Xue, Jing Wei, and Jie Xiang. Complexity Analysis of EEG, MEG, and fMRI in Mild Cognitive Impairment and Alzheimer's Disease: A Review. *Entropy*, 22(2):239, February 2020.

[30] Adam L. Halberstadt. Recent advances in the neuropsychopharmacology of serotonergic hallucinogens. *Behavioural Brain Research*, 277:99–120, January 2015.

[31] RL Carhart-Harris. The entropic brain — revisited. *Neuropharmacology*, 142(167–178), 2018.

[32] Giulio Ruffini, Giada Damiani, Diego Lozano-Soldevilla, Nikolas Deco, Fernando E Rosas, Narsis A Kiani, Adrián Ponce-Alvarez, Morten L Kringelbach, Robin Carhart-Harris, and Gustavo Deco. LSD-induced increase of Ising temperature and algorithmic complexity of brain dynamics. *Plos Computational Biology*, 19(2):e1010811, February 2023.

[33] María Eugenía López, Ricardo Bruna, Sara Aurtenetxe, José Ángel Pineda-Pardo, Alberto Marcos, Juan Arrazola, Ana Isabel Reinoso, Pedro Montejo, Ricardo Bajo, and Fernando Maestú. Alpha-band hypersynchronization in progressive mild cognitive impairment: a magnetoencephalography study. *Journal of Neuroscience*, 34(44):14551–14559, 2014.

[34] S. Passero, R. Rocchi, G. Vatti, L. Burgalassi, and N. Battistini. Quantitative EEG mapping, regional cerebral blood flow, and neuropsychological function in Alzheimer's disease. *Dementia (Basel, Switzerland)*, 6(3):148–156, 1995.

[35] Christopher S. Y. Benwell, Paula Davila-Pérez, Peter J. Fried, Richard N. Jones, Thomas G. Travison, Emiliano Santarnecchi, Alvaro Pascual-Leone, and Mouhsin M. Shafi. EEG spectral power abnormalities and their relationship with cognitive dysfunction in patients with Alzheimer's disease and type 2 diabetes. *Neurobiology of Aging*, 85:83–95, January 2020.

[36] Ruofan Wang, Jiang Wang, Haitao Yu, Xile Wei, Chen Yang, and Bin Deng. Power spectral density and coherence analysis of Alzheimer's EEG. *Cognitive Neurodynamics*, 9(3):291–304, June 2015.

[37] Michael Kometer, André Schmidt, Lutz Jäncke, and Franz X. Vollenweider. Activation of serotonin 2A receptors underlies the psilocybin-induced effects on α oscillations, N170 visual-evoked potentials, and visual hallucinations. *The Journal of Neuroscience: The Official Journal of the Society for Neuroscience*, 33(25):10544–10551, June 2013.

[38] Carla Pallavicini, Martina G. Vilas, Mirta Villarreal, Federico Zamberlan, Suresh Muthukumaraswamy, David Nutt, Robin Carhart-Harris, and Enzo Tagliazucchi. Spectral signatures of serotonergic psychedelics and glutamatergic dissociatives. *NeuroImage*, 200:281–291, October 2019.

[39] R L Carhart-Harris and K J Friston. REBUS and the anarchic brain: Toward a unified model of the brain action of psychedelics. *Pharmacological Reviews*, 71(3):316–344, July 2019.

[40] Claudio Babiloni, Katarzyna Blinowska, Laura Bonanni, Andrej Cichocki, Willem De Haan, Claudio Del Percio, Bruno Dubois, Javier Escudero, Alberto Fernández, Giovanni Frisoni, Bahar Guntekin, Mihaly Hajos, Harald Hampel, Emmanuel Ifeachor, Kerry Kilborn, Sanjeev Kumar, Kristinn Johnsen, Magnus Johannsson, Jaeseung Jeong, Fiona LeBeau, Roberta Lizio, Fernando Lopes da Silva, Fernando Maestú, William J. McGeown, Ian McKeith, Davide Vito Moretti, Flavio Nobili, John Olichney, Marco Onofrj, Jorge J. Palop, Michael Rowan, Fabrizio Stocchi, Zbigniew M. Struzik, Heikki Tanila, Stefan Teipel, John Paul Taylor, Marco Weiergräber, Gorsev Yener, Tracy Young-Pearse, Wilhelmus H. Drinkenburg, and Fiona Randall. What electrophysiology tells us about Alzheimer's disease: A window into the synchronization and connectivity of brain neurons. *Neurobiology of Aging*, 85:58–73, January 2020.

[41] Enzo Tagliazucchi, Leor Roseman, Mendel Kaelen, Csaba Orban, Suresh D. Muthukumaraswamy, Kevin Murphy, Helmut Laufs, Robert Leech, John McGonigle, Nicolas Crossley, Edward Bullmore, Tim Williams, Mark Bolstridge, Amanda Feilding, David J. Nutt, and Robin Carhart-Harris. Increased Global Functional Connectivity Correlates with LSD-Induced Ego Dissolution. *Current biology: CB*, 26(8):1043–1050, April 2016.

[42] Deco G. and Cruzat J. et al. Whole-brain multimodal neuroimaging model using serotonin receptor maps explains non-linear functional effects of lsd. *Curr Biol*, 28(19):3065–3074, 2018.

[43] Kringelbach M. L. and Cruzat J. et al. Dynamic coupling of whole-brain neuronal and neurotransmitter systems. *Proc Natl Acad Sci USA*, 117(17):9566–9576, 2020.

[44] Vohryzek J., Cabral J., Lord LD., Fernandes HM., Roseman L., Nutt DJ., Carhart-Harris RL., Deco G., and Kringelbach ML. Brain dynamics predictive of response to psilocybin for treatment-resistant depression. *Brain Communications*, 6(2):fcae049, 2024.

[45] Vohryzek J., Cabral J., Vuust P., Deco G., and Kringelbach ML. Understanding brain states across spacetime informed by whole-brain modelling. *Philosophical Transactions of the Royal Society A*, 380(2227):20210247, 2022.

[46] Herzog R., Mediano P. A. M., Rosas F. E., Lodder P., Carhart-Harris R., Perl Y. S., Tagliazucchi E., and Cofre R. A whole-brain model of the neural entropy increase elicited by psychedelic drugs. *Scientific reports*, 13(1):6244, 2023.

[47] Mindlin I. and Herzog R. et al. Whole-brain modelling supports the use of serotonergic psychedelics for the treatment of disorders of consciousness. *bioRxiv*, 2023.

[48] Jobst B. M., Atasoy S., Ponce-Alvarez A., Sanjuán A., Roseman L., Kaelen M., Carhart-Harris R., Kringelbach M. L., and Deco G. Increased sensitivity to strong perturbations in a whole-brain model of lsd. *Neuroimage*, 230:117809, 2021.

[49] Luppi A. I., Mediano P. A. M., Rosas F. E., Allanson J., Pickard J. D., Williams G. B., Craig M. M., Finoia P., Peattie A. R. D., Coppola P., et al. Whole-brain modelling identifies distinct but convergent paths to unconsciousness in anaesthesia and disorders of consciousness. *Communications biology*, 5(1):384, 2022.

[50] Jansen B. H. and Rit V. G. Electroencephalogram and visual evoked potential generation in a mathematical model of coupled cortical columns. *Biol Cybern*, 73(4):357–366, 1995.

[51] Cook B. J., Peterson A. D. H., Woldman W., and Terry J. R. Neural field models: A mathematical overview and unifying framework. *Mathematical Neuroscience and Applications*, 2, 2022.

[52] G. Ruffini, R. Sanchez-Todo, L. Dubreuil, R. Salvador, D. Pinotsis, E. K. Miller, F. Wendling, E. Santarnecchi, and A. Bastos. P118 A Biophysically realistic Laminar Neural Mass Modeling framework for transcranial Current Stimulation. *Clinical Neurophysiology*, 131(4):e78–e79, April 2020.

[53] Sanchez-Todo R. and Bastos A. M. et al. A physical neural mass model framework for the analysis of oscillatory generators from laminar electrophysiological recordings. *Neuroimage*, 270:119938, 2023.

[54] Roser Sanchez-Todo, Edmundo Lopez-Sola, Borja Mercadal, and Giulio Ruffini. Laminar Neural Mass Model for Representing Alzheimer's Disease Electrophysiopathology. *in prep*, 2024.

[55] Ruffini G., Modolo J., Sanchez-Todo R., Salvador R., and Santarnecchi E. *Clinical Drivers for Personalization of Transcranial Current Stimulation (tES 3.0)*, pages 353–370. Springer, 2020.

[56] Sanchez-Todo R., Salvador R., Santarnecchi E., Wendling F., Deco G., and Ruffini G. Personalization of hybrid brain models from neuroimaging and electrophysiology data. *bioRxiv*, 2018.

[57] Mercadal B., Lopez-Sola E., Galan-Gadea A., Al Harrach M., Sanchez-Todo R., Salvador R., Bartolomei F., Wendling F., and Ruffini G. Towards a mesoscale physical modeling framework for stereotactic-eeg recordings. *Journal of Neural Engineering*, 20(1):016005, 2023.

[58] Börgers C., Epstein S., and Kopell N. J. Gamma oscillations mediate stimulus competition and attentional selection in a cortical network model. *Proc Natl Acad Sci USA*, 105(46):18023–18028, 2008.

[59] Nunez P. L. and Srinivasan R. *Electric fields of the brain: the neurophysics of EEG*. Oxford University Press, USA, 2006.

[60] György Buzsáki, Costas A. Anastassiou, and Christof Koch. The origin of extracellular fields and currents — EEG, ECoG, LFP and spikes. *Nature Reviews Neuroscience*, 13(6):407–420, May 2012.

[61] Welch P. The use of fast fourier transform for the estimation of power spectra: A method based on time averaging over short, modified periodograms. *IEEE Transactions on Audio and Electroacoustics*, 15(2):70–73, 1967.

[62] Desikan R. S., Ségonne F., Fischl B., Quinn B. T., Dickerson B. C., Blacker D., Buckner R. L., Dale A. M., Maguire R. P., Hyman B. T., et al. An automated labeling system for subdividing the human cerebral cortex on mri scans into gyral based regions of interest. *Neuroimage*, 31(3):968–980, 2006.

[63] Fischl B., Van Der Kouwe A., Destrieux C., Halgren E., Ségonne F., Salat D. H., Busa E., Seidman L. J., Goldstein J., Kennedy D., et al. Automatically parcellating the human cerebral cortex. *Cerebral cortex*, 14(1):11–22, 2004.

[64] J-Donald Tournier, Robert Smith, David Raffelt, Rami Tabbara, Thijs Dhollander, Maximilian Pietsch, Daan Christiaens, Ben Jeurissen, Chun-Hung Yeh, and Connelly Alan. Mrtrix3: A fast, flexible and open software framework for medical image processing and visualisation. *Neuroimage*, 202:116–137, 2019.

[65] Oscar Esteban, Christopher J Markiewicz, Ross W Blair, Craig A Moodie, A Ilkay Isik, Asier Erramuzpe, James D Kent, Mathias Goncalves, Elizabeth

DuPre, Madeleine Snyder, et al. fmriprep: a robust preprocessing pipeline for functional mri. *Nature methods*, 16(1):111–116, 2019.

[66] Krzysztof Gorgolewski, Christopher D Burns, Cindee Madison, Dav Clark, Yaroslav O Halchenko, Michael L Waskom, and Satrajit S Ghosh. Nipype: a flexible, lightweight and extensible neuroimaging data processing framework in python. *Frontiers in neuroinformatics*, 5:12318, 2011.

[67] Avants BB, Tustison N, and Song G. Advanced normalization tools (ants). *Insight j*, 2 (365):1–35, 2009.

[68] Friston K. J., Mechelli A., Turner R., and Price C. J. Nonlinear responses in fmri: the balloon model, volterra kernels, and other hemodynamics. *NeuroImage*, 12(4):466–477, 2000.

[69] Beliveau V., Ganz M., Feng L., Ozenne B., Højgaard L., Fisher P. M., Svarer C., Greve D. N., and Knudsen G. M. A high-resolution in vivo atlas of the human brain's serotonin system. *Journal of Neuroscience*, 37(1):120–128, 2017.

[70] PC Miranda, A Mekonnen, R Salvador, and G Ruffini. The electric field in the cortex during transcranial current stimulation. *Neuroimage*, 70:48–58, 2013.

[71] Giulio Ruffini, Fabrice Wendling, Isabelle Merlet, Behnam Molaee-Ardekani, Abeye Mekonnen, Ricardo Salvador, Aureli Soria-Frisch, Carles Grau, Stephen Dunne, and Pedro C. Miranda. Transcranial Current Brain Stimulation (tCS): Models and Technologies. *IEEE Transactions on Neural Systems and Rehabilitation Engineering*, 21(3):333–345, May 2013.

[72] Giulio Ruffini, Michael D Fox, Oscar Ripolles, Pedro Cavaleiro Miranda, and Alvaro Pascual-Leone. Optimization of multifocal transcranial current stimulation for weighted cortical pattern targeting from realistic modeling of electric fields. *Neuroimage*, 89:216–225, 2014.

[73] Buzsáki G., Anastassiou C. A., and Koch C. The origin of extracellular fields and currents—eeg, ecog, lfp and spikes. *Nature reviews neuroscience*, 13(6):407–420, 2012.

[74] Giulio Ruffini. Lempel-Zip Complexity Reference, July 2017.

[75] Giulio Ruffini, David Ibañez, Eleni Kroupi, Jean-François Gagnon, Jacques Montplaisir, Ronald B Postuma, Marta Castellano, and Aureli Soria-Frisch. Algorithmic complexity of eeg for prognosis of neurodegeneration in idiopathic rapid eye movement behavior disorder (rbd). *Annals of biomedical engineering*, 47:282–296, 2019.

[76] Thomas M Cover. *Elements of information theory*. John Wiley & Sons, 1999.

[77] Terry A. Welch. A technique for high-performance data compression. *Computer*, 17(06):8–19, 1984.

[78] Benedikt Zott, Manuel M. Simon, Wei Hong, Felix Unger, Hsing-Jung Chen-Engerer, Matthew P. Frosch, Bert Sakmann, Dominic M. Walsh, and Arthur

Konnerth. A vicious cycle of β amyloid-dependent neuronal hyperactivation. *Science (New York, N.Y.)*, 365(6453):559–565, August 2019.

[79] Yifei Bao, Xin Yang, Yi Fu, Zhengyan Li, Ru Gong, and Wei Lu. NMDAR-dependent somatic potentiation of synaptic inputs is correlated with β amyloid-mediated neuronal hyperactivity. *Translational Neurodegeneration*, 10(1):34, September 2021.

[80] Samuel S. Harris, Fred Wolf, Bart De Strooper, and Marc Aurel Busche. Tipping the Scales: Peptide-Dependent Dysregulation of Neural Circuit Dynamics in Alzheimer's Disease. *Neuron*, 107(3):417–435, August 2020.

[81] Ruffini G., Lopez-Sola E., Vohryzek J., and Sanchez-Todo R. Neural geometrodynamics, complexity, and plasticity: a psychedelics perspective. *Entropy*, 26(1), 2024.

[82] Giulia Sprugnoli, Fanny Munsch, Davide Cappon, Rachel Paciorek, Joanna Macone, Ann Connor, Georges El Fakhri, Ricardo Salvador, Giulio Ruffini, Kevin Donohoe, Mouhsin M. Shafi, Daniel Press, David C. Alsop, Alvaro Pascual Leone, and Emiliano Santarnecchi. Impact of multisession 40Hz tACS on hippocampal perfusion in patients with Alzheimer's disease. *Alzheimer's Research & Therapy*, 13(1):203, December 2021.

[83] Maeva Dhaynaut, Giulia Sprugnoli, Davide Cappon, Joanna Macone, Justin S. Sanchez, Marc D. Normandin, Nicolas J. Guehl, Giacomo Koch, Rachel Paciorek, Ann Connor, Daniel Press, Keith Johnson, Alvaro Pascual-Leone, Georges El Fakhri, and Emiliano Santarnecchi. Impact of 40 Hz Transcranial Alternating Current Stimulation on Cerebral Tau Burden in Patients with Alzheimer's Disease: A Case Series. *Journal of Alzheimer's disease: JAD*, 85(4):1667–1676, 2022.

[84] Hannah F. Iaccarino, Annabelle C. Singer, Anthony J. Martorell, Andrii Rudenko, Fan Gao, Tyler Z. Gillingham, Hansruedi Mathys, Jinsoo Seo, Oleg Kritskiy, Fatema Abdurrob, Chinnakkaruppan Adaikkan, Rebecca G. Canter, Richard Rueda, Emery N. Brown, Edward S. Boyden, and Li-Huei Tsai. Gamma frequency entrainment attenuates amyloid load and modifies microglia. *Nature*, 540(7632):230–235, December 2016.

[85] Anthony J. Martorell, Abigail L. Paulson, Ho-Jun Suk, Fatema Abdurrob, Gabrielle T. Drummond, Webster Guan, Jennie Z. Young, David Nam-Woo Kim, Oleg Kritskiy, Scarlett J. Barker, Vamsi Mangena, Stephanie M. Prince, Emery N. Brown, Kwanghun Chung, Edward S. Boyden, Annabelle C. Singer, and Li-Huei Tsai. Multi-sensory Gamma Stimulation Ameliorates Alzheimer's-Associated Pathology and Improves Cognition. *Cell*, 177(2):256–271.e22, April 2019.

[86] Chinnakkaruppan Adaikkan, Steven J. Middleton, Asaf Marco, Ping-Chieh Pao, Hansruedi Mathys, David Nam-Woo Kim, Fan Gao, Jennie Z. Young, Ho-Jun Suk, Edward S. Boyden, Thomas J. McHugh, and Li-Huei Tsai. Gamma

Entrainment Binds Higher-Order Brain Regions and Offers Neuroprotection. *Neuron*, 102(5):929–943.e8, June 2019.

[87] Chinnakkaruppan Adaikkan and Li-Huei Tsai. Gamma Entrainment: Impact on Neurocircuits, Glia, and Therapeutic Opportunities. *Trends in Neurosciences*, 43(1):24–41, January 2020.

[88] Giulio Ruffini, Francesca Castaldo, Edmundo Lopez-Sola, Roser Sanchez-Todo, and Jakub Vohryzek. The algorithmic agent perspective and computational neuropsychiatry: From etiology to advanced therapy in major depressive disorder. *PsyArXiv*, March 2024.

[89] Reisa A. Sperling, Paul S. Aisen, Laurel A. Beckett, David A. Bennett, Suzanne Craft, Anne M. Fagan, Takeshi Iwatsubo, Clifford R. Jack, Jeffrey Kaye, Thomas J. Montine, Denise C. Park, Eric M. Reiman, Christopher C. Rowe, Eric Siemers, Yaakov Stern, Kristine Yaffe, Maria C. Carrillo, Bill Thies, Marcelle Morrison-Bogorad, Molly V. Wagster, and Creighton H. Phelps. Toward defining the preclinical stages of Alzheimer's disease: Recommendations from the National Institute on Aging-Alzheimer's Association workgroups on diagnostic guidelines for Alzheimer's disease. *Alzheimer's & Dementia: The Journal of the Alzheimer's Association*, 7(3):280–292, May 2011.

[90] R. C. Petersen. Mild cognitive impairment as a diagnostic entity. *Journal of Internal Medicine*, 256(3):183–194, September 2004.

[91] Alzheimer's Association. 2020 Alzheimer's disease facts and figures. *Alzheimer's & Dementia: The Journal of the Alzheimer's Association*, March 2020.

[92] Elias P. Casula, Maria C. Pellicciari, Sonia Bonnì, Ilaria Borghi, Michele Maiella, Martina Assogna, Marilena Minei, Caterina Motta, Alessia D'Acunto, Francesco Porrazzini, Valentina Pezzopane, Lucia Mencarelli, Andrea Roncaioli, Lorenzo Rocchi, Danny A. Spampinato, Carlo Caltagirone, Emiliano Santarnecchi, Alessandro Martorana, and Giacomo Koch. Decreased Frontal Gamma Activity in Alzheimer Disease Patients. *Annals of Neurology*, 92(3):464, July 2022.

[93] David López-Sanz, Ricardo Bruña, Pilar Garcés, Carmen Camara, Noelia Serrano, Inmaculada Concepción Rodríguez-Rojo, ML Delgado, M Montenegro, Ramón López-Higes, Miguel Yus, et al. Alpha band disruption in the ad-continuum starts in the subjective cognitive decline stage: a meg study. *Scientific reports*, 6(1):37685, 2016.

[94] Delphine Puttaert, Vincent Wens, Patrick Fery, Antonin Rovai, Nicola Trotta, Nicolas Coquelet, Sandra De Breucker, Niloufar Sadeghi, Tim Coolen, Serge Goldman, Philippe Peigneux, Jean-Christophe Bier, and Xavier De Tiège. Decreased Alpha Peak Frequency Is Linked to Episodic Memory Impairment in Pathological Aging. *Frontiers in Aging Neuroscience*, 13, August 2021.

[95] Seyyedeh Nahaleh Fatemi, Mohammad Javad Sedghizadeh, and Hamid Aghajan. Theta-gamma phase-amplitude coupling explains the advantage of audi-

tory plus visual gamma entrainment in Alzheimer's therapy. *Alzheimer's & Dementia*, 17(S7):e053451, 2021.

[96] Brian H. Silverstein, Nicholas Kolbman, Amanda Nelson, Tiecheng Liu, Peter Guzzo, Jim Gilligan, UnCheol Lee, George A. Mashour, Giancarlo Vanini, and Dinesh Pal. Psilocybin induces dose-dependent changes in functional network organization in rat cortex, February 2024.

[97] Suresh D. Muthukumaraswamy, Robin L. Carhart-Harris, Rosalyn J. Moran, Matthew J. Brookes, Tim M. Williams, David Errtizoe, Ben Sessa, Andreas Papadopoulos, Mark Bolstridge, Krish D. Singh, Amanda Feilding, Karl J. Friston, and David J. Nutt. Broadband Cortical Desynchronization Underlies the Human Psychedelic State. *Journal of Neuroscience*, 33(38):15171–15183, September 2013.

[98] Bastos A. M., Usrey W. M., Adams R. A., Mangun G. R., Fries P., and Friston K. J. Canonical microcircuits for predictive coding. *Neuron*, 76(4):695–711, 2012.

[99] Mejias J. F., Murray J. D., Kennedy H., and Wang X. Feedforward and feedback frequency-dependent interactions in a large-scale laminar network of the primate cortex. *Science advances*, 2(11):e1601335, 2016.

[100] Jaramillo J., Mejias J. F., and Wang X. Engagement of pulvino-cortical feedforward and feedback pathways in cognitive computations. *Neuron*, 101(2):321–336, 2019.

[101] Uddin L. Q., Mooshagian E., Zaidel E., Scheres A., Margulies D. S., Kelly A. M. C., Shehzad Z., Adelstein J. S., Castellanos F. X., Biswal B. B., et al. Residual functional connectivity in the split-brain revealed with resting-state functional mri. *Neuroreport*, 19(7):703–709, 2008.

[102] Wang X., Leong A. T. L., Chan R. W., Liu Y., and Wu E. X. Thalamic low frequency activity facilitates resting-state cortical interhemispheric mri functional connectivity. *Neuroimage*, 201:115985, 2019.

[103] Müller F., Lenz C., Dolder P., Lang U., Schmidt A., Liechti M., and Borgwardt S. Increased thalamic resting-state connectivity as a core driver of lsd-induced hallucinations. *Acta Psychiatrica Scandinavica*, 136(6):648–657, 2017.

[104] Markello R. D., Hansen J. Y., Liu Z., Bazinet V., Shafiei G., Suárez L. E., Blostein N., Seidlitz J., Baillet S., Satterthwaite T. D., et al. Neuromaps: structural and functional interpretation of brain maps. *Nature Methods*, 19(11):1472–1479, 2022.

[105] Fischl B. Freesurfer. *Neuroimage*, 62(2):774–781, 2012.

[106] Olaf Ronneberger, Philipp Fischer, and Thomas Brox. U-net: Convolutional networks for biomedical image segmentation. In Nassir Navab, Joachim Hornegger, William M. Wells, and Alejandro F. Frangi, editors, *Medical Image Computing and Computer-Assisted Intervention – MICCAI 2015*, pages 234–241, Cham, 2015. Springer International Publishing.

[107] Valer Jurcak, Daisuke Tsuzuki, and Ippeita Dan. 10/20, 10/10, and 10/5 systems revisited: Their validity as relative head-surface-based positioning systems. *NeuroImage*, 34(4):1600–1611, 2007.

[108] Ruffini G. Application of the reciprocity theorem to eeg inversion and optimization of eeg-driven transcranial current stimulation (tcs, including tdcs, tacs, trns). *arXiv*, 2015.

[109] R Salvador, MC Biagi, M Pérez Pelegrí, J Zhou, T Travison, A Pascual-Leone, B Manor, and G Ruffini. Towards the identification and optimization of the "dose-response" relationship of transcranial direct current stimulation. *bioRxiv*, pages 2022–01, 2022.

Supplementary Information

S.1 Potential therapeutic effects of psychedelics in AD

Stages of AD and electrophysiological alterations

AD progresses through distinct stages, beginning with a *preclinical* phase, characterized by pathological changes such as amyloid-beta and tau accumulation detectable through biomarkers, but without noticeable cognitive symptoms.[89] The next stage, *prodromal AD* or Mild Cognitive Impairment (MCI) due to AD, involves subtle cognitive declines, particularly in memory, that exceed normal aging but do not yet significantly impair daily life.[90] The disease progresses then from *mild AD dementia*, where cognitive impairments interfere with daily tasks, to *moderate AD dementia* with severe cognitive decline and increased dependency, and ultimately to *severe AD dementia* marked by extensive neurodegeneration.[91]

In the preclinical stages of AD, some studies report an increase in alpha power along with a potential increase in gamma power.[20,22] However, findings regarding gamma power in this stage are variable, with some evidence suggesting stable or mildly reduced gamma activity.[23]

After the preclinical stage of AD, the EEG spectrum undergoes a characteristic slowing, with increased power in lower frequencies (delta, theta) and decreased power in higher frequencies (beta and gamma bands) as the disease progresses.[24,40,92] Increased alpha power and hypersynchronization in alpha-band functional connectivity (FC) reflect an imbalance in excitation and inhibition, which contributes to neuronal hyperactivity and network disruptions,[20,33] although there is also evidence of decreased alpha power in MCI patients.[93]

As the disease advances into early to moderate AD, alpha power begins to decline, and a slowing of the alpha peak frequency is observed, which correlates with structural and functional impairments.[27,34,94] Gamma oscillations, which are essential for higher-order cognitive functions like working memory and sensory processing, show a more consistent decrease during MCI and early AD, reflecting synaptic dysfunction and impaired connectivity.[24,40,54]

In later stages of AD, both alpha and gamma power are markedly reduced, alongside significant increases in slower rhythms such as delta and theta. This shift in the EEG power spectrum mirrors widespread cortical atrophy, disrupted excitatory-inhibitory balance, and breakdowns in network synchronization and efficiency, which underpin the severity of cognitive and functional decline.[40,92]

Physiopathology of AD

AD is associated with the dysfunction of inhibitory interneurons, particularly those expressing parvalbumin (PV), and the resulting network abnormalities in AD.[25,54] PV interneurons, crucial for maintaining fast oscillations, become impaired in AD due to both direct pathology and, possibly, compensatory neural changes.[25] This dysfunction leads to a loss of gamma rhythm, essential for higher cognitive processes,

and contributes to network instability and hypersynchrony in slower frequencies.

In early AD, synaptic connections from PV interneurons in superficial layers—critical for generating fast gamma rhythms—are among the first to be disrupted. This early damage corresponds with the emergence of increased alpha and reduced gamma activity observed in MCI and mild-to-moderate AD. Eventually, persistent alpha hypersynchronization further deteriorates these circuits and affects other connected areas in later disease stages. While the precise mechanisms linking PV interneuron dysfunction to EEG slowing remain unclear, and compensatory processes have been suggested,[22] a modified version of LaNMM demonstrates how disrupting PV synapse connectivity can reproduce these electrophysiological changes.[54] In this model, slowing of the EEG emerges from the interaction between disrupted fast circuits and slow circuits rather than compensation.

Restoring healthy oscillatory balance

Recent research suggests that restoring PV interneuron function or modulating network synchrony could help re-establish healthy oscillatory dynamics and improve cognitive function in AD, which motivates the use of gamma stimulation in AD, for instance, through sensory stimuli or transcranial alternating current stimulation (tACS).[25,54,84,85,95] Building on this idea, psychedelics could restore the oscillatory balance in AD, especially in the early stages of the disease. Psychedelics reduce alpha power, enhancing network flexibility and interconnectivity,[1,8] and may increase gamma power, promoting global connectivity and enhancing oscillations associated with cognitive processing.[19,37,96,97] By modulating 5-HT2A receptors on cortical pyramidal cells, these compounds may indirectly engage PV interneurons, promoting gamma synchrony and balancing excitatory-inhibitory networks.[30] Gamma power increases through psychedelics could potentially counteract the reduction observed in AD, further aiding in the restoration of cognitive functions that depend on these rhythms. Psychedelics also reduce delta and theta activity, counteracting the increased power in these bands often observed in AD.[38] This modulation of slow oscillations may help attenuate pathological hypersynchrony in delta and theta bands, restoring a healthier balance across frequencies that aligns with normal cognitive processing.

The enhanced excitation under psychedelics is also related to increased neural entropy and complexity of ongoing brain activity, as reported extensively in the literature,[8,32] which could counteract the reduction in complexity observed in AD subjects.[28,29] Psychedelics also modulate network connectivity patterns, increasing global integration and decreasing modularity.[41] This shift could address the network decoupling seen in AD, promoting a healthier, more flexible connectivity pattern. The combined effects on gamma power, slow oscillations, and network integration suggest that psychedelics may help re-establish synchronous activity and alleviate cognitive deficits through PV interneuron engagement, oscillatory enhancement, and network stabilization. This rationale motivates the study of psychedelics as potential modulators of oscillatory dynamics and connectivity, addressing key electrophysiological deficits associated with disease progression and cognitive impairment.

S.2 LaNMM description

S.2.1 Single LaNMM equations and parameters

The LaNMM[53] employs a second-order differential equation to model the average membrane potential perturbation in a neuronal population m caused by inputs from another population n. This equation captures the synaptic dynamics within the average neuron of a given population, translating the presynaptic mean firing rate φ_n into a perturbation of the mean membrane potential $u_{m\leftarrow n}$ in the postsynaptic population m. This relationship is expressed through the integral operator $\hat{L}^{-1}_{m\leftarrow n}$, defined as:

$$u_{m\leftarrow n}(t) = \hat{L}^{-1}_{m\leftarrow n}[C_{m\leftarrow n}\varphi_n(t)] \tag{S1}$$

where $C_{m\leftarrow n}$ is the connectivity constant, indicating the average number of synaptic contacts between population types, which inverse is the differential operator $\hat{L}_{m\leftarrow n}[u_{m\leftarrow n}(t)] = C_{m\leftarrow n}\varphi_n(t)$, defined as

$$\hat{L}_s[u_s(t)] = \frac{1}{A_s}\left(\frac{1}{a_s}\frac{d^2}{dt^2} + 2\frac{d}{dt} + a_s\right)u_s(t) \tag{S2}$$

where A_s is the average excitatory/inhibitory synaptic gain and a_s is the rate constant of the connection ($a_s = 1/\tau_s$, τ_s denoting the synaptic time constant). Note that, for simplicity, the single index s is used to represent each average synapse (i.e., connection) from one neuronal population to another, so that $s \equiv \{m \leftarrow n : C_{m\leftarrow n} \neq 0\}$. In the LaNMM, $s \in [1, 13]$ and the neural populations are denoted by $(m, n) \in [P_1, \mathrm{SS}, \mathrm{SST}, P_2, \mathrm{PV}, e1, e2]$. The indices assigned to each connection in the LaNMM are depicted in Fig. S1. Finally, the average output firing rate φ_m of population m is defined by the sigmoid function

$$\varphi_m(t) = \sigma_m\big(\nu_m(t)\big) = \frac{2\varphi_0}{1 + e^{r(\nu_0 - \nu_m(t))}} \tag{S3}$$

where φ_0 is half of the maximum firing rate of the population, ν_0 the value of the potential when the firing rate is φ_0 and r determines the slope of the sigmoid at the central symmetry point (ν_0,φ_0). Here, ν_m denotes the average membrane potential of the postsynaptic population m

$$\nu_m(t) = \sum_s u_s(t) \tag{S4}$$

where u_s is the membrane perturbation per each of its incoming connections s. Consequently, the general differential equation capturing the average synaptic dynamics of each connection s in the LaNMM between each postsynaptic and presynaptic population pair $m \leftarrow n$ is defined as

$$C_s\varphi_n(t) = \frac{1}{A_s}\left(\frac{1}{a_s}\frac{d^2}{dt^2} + 2\frac{d}{dt} + a_s\right)u_s(t) \tag{S5}$$

which depends on the average membrane potential perturbation caused by each connection u_s inputting the presynaptic population n, and the average membrane potential ν_n and average firing rate φ_n of this presynaptic population.

Notice that this modeling approach focuses on the dynamics of the connections between neural populations instead of the populations' dynamics, as opposed to the traditional approach followed in neural mass modeling. This is referred to by Sanchez-Todo et al. (2023)[53] as the *synapse-driven* formulation of an NMM, which simplifies the definition of the neural dynamics generalizing the model equations. The equation for each connection describing the LaNMM is shown hereafter:

$$
\begin{aligned}
\hat{L}_1[u_1(t)] &= C_1\sigma_{SS}(\nu_{SS}) = \frac{1}{A_1}\left(\frac{1}{a_1}\frac{d^2}{dt^2} + 2\frac{d}{dt} + a_1\right)u_1(t) \\
\hat{L}_2[u_2(t)] &= C_2\sigma_{SST}(\nu_{SST}) = \frac{1}{A_2}\left(\frac{1}{a_2}\frac{d^2}{dt^2} + 2\frac{d}{dt} + a_2\right)u_2(t) \\
\hat{L}_3[u_3(t)] &= C_3\varphi_{e1} = \frac{1}{A_3}\left(\frac{1}{a_3}\frac{d^2}{dt^2} + 2\frac{d}{dt} + a_3\right)u_3(t) \\
\hat{L}_4[u_4(t)] &= C_4\sigma_{P_1}(\nu_{P_1}) = \frac{1}{A_4}\left(\frac{1}{a_4}\frac{d^2}{dt^2} + 2\frac{d}{dt} + a_4\right)u_4(t) \\
\hat{L}_5[u_5(t)] &= C_5\sigma_{P_1}(\nu_{P_1}) = \frac{1}{A_5}\left(\frac{1}{a_5}\frac{d^2}{dt^2} + 2\frac{d}{dt} + a_5\right)u_5(t) \\
\hat{L}_6[u_6(t)] &= C_6\sigma_{P_2}(\nu_{P_2}) = \frac{1}{A_6}\left(\frac{1}{a_6}\frac{d^2}{dt^2} + 2\frac{d}{dt} + a_6\right)u_6(t) \\
\hat{L}_7[u_7(t)] &= C_7\sigma_{PV}(\nu_{PV}) = \frac{1}{A_7}\left(\frac{1}{a_7}\frac{d^2}{dt^2} + 2\frac{d}{dt} + a_7\right)u_7(t) \\
\hat{L}_8[u_8(t)] &= C_8\varphi_{e2} = \frac{1}{A_8}\left(\frac{1}{a_8}\frac{d^2}{dt^2} + 2\frac{d}{dt} + a_8\right)u_8(t) \\
\hat{L}_9[u_9(t)] &= C_9\sigma_{P_2}(\nu_{P_2}) = \frac{1}{A_9}\left(\frac{1}{a_9}\frac{d^2}{dt^2} + 2\frac{d}{dt} + a_9\right)u_9(t) \\
\hat{L}_{10}[u_{10}(t)] &= C_{10}\sigma_{PV}(\nu_{PV}) = \frac{1}{A_{10}}\left(\frac{1}{a_{10}}\frac{d^2}{dt^2} + 2\frac{d}{dt} + a_{10}\right)u_{10}(t) \\
\hat{L}_{11}[u_{11}(t)] &= C_{11}\sigma_{P_2}(\nu_{P_2}) = \frac{1}{A_{11}}\left(\frac{1}{a_{11}}\frac{d^2}{dt^2} + 2\frac{d}{dt} + a_{11}\right)u_{11}(t) \\
\hat{L}_{12}[u_{12}(t)] &= C_{12}\sigma_{P_1}(\nu_{P_1}) = \frac{1}{A_{12}}\left(\frac{1}{a_{12}}\frac{d^2}{dt^2} + 2\frac{d}{dt} + a_{12}\right)u_{12}(t) \\
\hat{L}_{13}[u_{13}(t)] &= C_{13}\sigma_{P_1}(\nu_{P_1}) = \frac{1}{A_{13}}\left(\frac{1}{a_{13}}\frac{d^2}{dt^2} + 2\frac{d}{dt} + a_{13}\right)u_{13}(t)
\end{aligned}
$$

with the average membrane potentials ν_m of each neural population in the LaNMM being given by

$$
\begin{aligned}
\nu_{P_1} &= u_1 + u_2 + u_3 + u_{11} \\
\nu_{SS} &= u_4 \\
\nu_{SST} &= u_5 \\
\nu_{P_2} &= u_6 + u_7 + u_8 + u_{12} \\
\nu_{PV} &= u_9 + u_{10} + u_{13}
\end{aligned}
$$

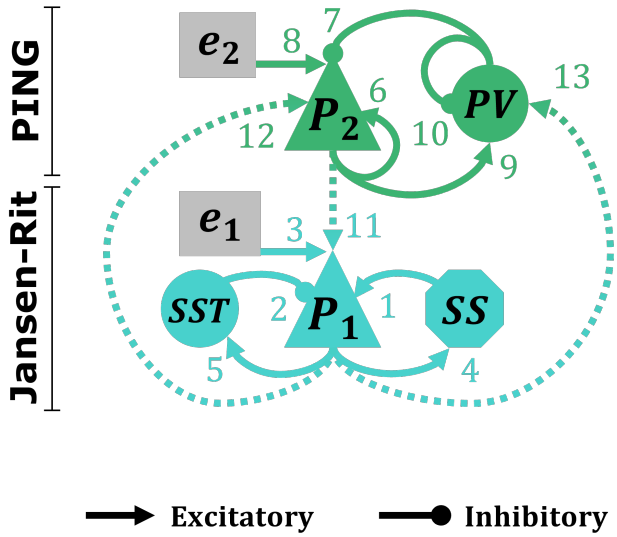

Figure S1: Schematic diagram of the LaNMM depicting its neuronal populations and the connections between them. PING model (green) and JR model (blue). Rounded shapes indicate inhibitory populations and interactions, triangles and octagons indicate excitatory ones, and squares represent external inputs. Numbers indicate the index s assigned to each connection. Dashed lines represent connections between the PING and Jansen-Rit parts sub-circuits. The neural population abbreviations (P_1, SS, SST, P_2, PV, $e1$, $e2$) are defined in the main text.

The list of LaNMM parameters used for the simulations is shown in Table S1. Model parameters were adopted from Sanchez-Todo et al.,[53] except for the standard deviation σ_e of the external noisy perturbations e_1 and e_2. In the single LaNMM study, we adjusted σ_e to match the average SD value of the external inputs received by each LaNMM in the whole-brain model personalization (see Section S.2.3).

S.2.2 Long-range LaNMM connectivity

The long-range connections between nodes in the model are weighted following the connectivity patterns between cortical regions described by Bastos et al.[98] and recent modeling work.[99,100] In particular, P_1 and P_2 populations of different parcels i, j are connected as follows: $P_1^i \rightarrow P_1^j$ (lateral connection), $P_1^i \rightarrow P_2^j$ (feedback or descending connection) and $P_2^i \rightarrow P_2^j$ (feedforward or ascending connection) with relative weights w of 0.5, 0.5 and 1 respectively (see Figure S2). The resulting connectivity C_{ij} between parcels i and j depends which of these three connections is involved, and is computed as:

$$C_{ij} = w \cdot G \cdot K_{ij} \tag{S6}$$

w represents the relative strength of the connection, G is the global scaling factor that adjusts the overall connection strength and K_{ij} is the connectome value. For simplicity, we assumed that all long-range cortico-cortical connections across brain columns are mediated via pyramidal populations — hence, they all have an excitatory effect.

Parameter	Description	Value
A_s	Average excitatory and (fast and slow) inhibitory synaptic gains	$A_{\text{AMPA}} = 3.25$ mV, $A_{\text{GABA}_{\text{fast}}} = -22$ mV, $A_{\text{GABA}_{\text{slow}}} = -30$ mV
a_s	Time constant of average excitatory and inhibitory postsynaptic potentials	$a_{\text{AMPA}} = 100$ Hz, $a_{\text{GABA}_{\text{fast}}} = 50$ Hz, $a_{\text{GABA}_{\text{slow}}} = 220$ Hz
C_s	Connectivity constant between populations	$C_1 = 108, C_2 = 33.7$, $C_3 = 1, C_4 = 135$, $C_5 = 33.75, C_6 = 70$, $C_7 = 550, C_8 = 1$, $C_9 = 200, C_{10} = 100$, $C_{11} = 80, C_{12} = 200$, $C_{13} = 30$
ν_0	Potential at 50 % of the firing rate	6 mV (except P_2's $\nu_0 = 1$ mV)
φ_0	Half of the maximum firing rate	2.5 Hz
r	Slope of the sigmoid function at v_0	0.56 mV^{-1}
μ_e, σ_e	Mean and SD of the external input firing rates φ_e	φ_{e1}: white noise with $\mu_{e1} = 270$ Hz and $\sigma_{e1} = 34$ Hz φ_{e2}: white noise with $\mu_{e2} = 90$ Hz and $\sigma_{e2} = 34$ Hz

Table S1: Parameters, description, and values of the baseline Laminar NMM employed in this work. The values are taken from Sanchez-Todo et al.,[53] except for the external inputs (φ_{e1}, φ_{e2}). Notice that the sigmoid function parameters defining the firing rate φ_m in this model (ν_0, φ_0, r), apply to all neuron populations. Moreover, all excitatory connections follow the same synapse dynamics, $(A, a)_{\text{AMPA}} = (A, a)_{1,3,4,5,6,8,9,11,12,13}$ while all inhibitory connections follow either fast, $(A, a)_{\text{GABA}_{\text{fast}}} = (A, a)_{7,10}$, or slow dynamics, $(A, a)_{\text{GABA}_{\text{slow}}} = (A, a)_2$.

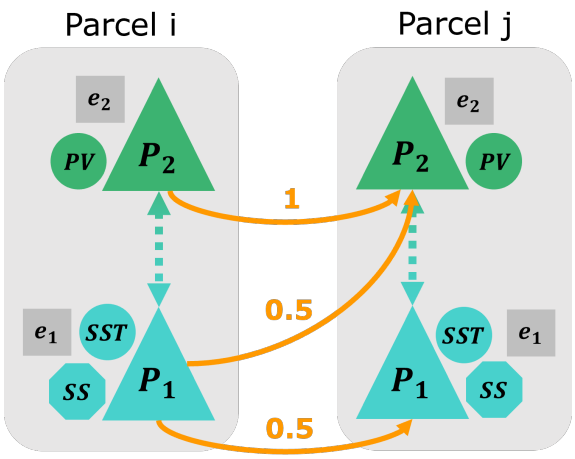

Figure S2: Long-range cortico-cortical parcel connections and their relative strength. Note that, for simplicity, cortico-cortical connections are only drawn in one direction, but they are present in both directions in the model.

S.2.3 Whole-brain model external inputs

The external noisy inputs $e1$ and $e2$ applied to the JR and PING model's pyramidal populations (see Section 2.1) are modeled in the whole-brain models as the sum of two additive noises:

- On the one hand, a *common noise* is applied homogeneously to all parcels (i.e., the same realization of noise is applied to every parcel) and modeled as white Gaussian noise with mean $\mu_{c1} = 270$ Hz to P_1 and mean $\mu_{c2} = 90$ Hz to P_2, mirroring the values of the single LaNMM.[53] The SD of the common noise σ_c is personalized for every subject.
- On top of this, white Gaussian noise with mean $\mu_i = 0$ Hz and SD $\sigma_i = 20$ Hz is added to the common noise in both P_1 and P_2 *homotopically*, i.e., the same realization of noise is applied to "mirror" areas of homologous parcels in both hemispheres—e.g., same noise realization to the left and right insula.

These two external inputs model the influence of FC pathways involving subcortical structures such as the thalamus,[101,102] constituting a rough thalamo-cortical model, which may play a pivotal role in the context of psychedelics.[103]

S.3 Parcellation of PET-derived 5-HT2AR density in DK-68

To obtain a quantitative measure of the 5-HT2AR density in each DK-68 parcel, we parcellated Beliveau et al.'s 5-HT2AR average density map into the DK-68 cortical atlas. For this purpose, we used the *Neuromaps* toolbox[104] and followed Hansen et al.'s parcellation pipeline.[11] We used the DK-68 average subject template atlas automatically labeled by FreeSurfer 7.4 in *fsaverage* space[63,105] to obtain the average 5-HT2AR density in the surface area of each cortical parcel. The PET imaging data used in this study, including receptor images and densities, are included in Neuromaps [*] and the DK-68 *fsaverage* atlas is available in the installation files of *FreeSurfer* 7.4[†]. The obtained receptor map and the DK-68 parcellation used can be found in Figure S3.

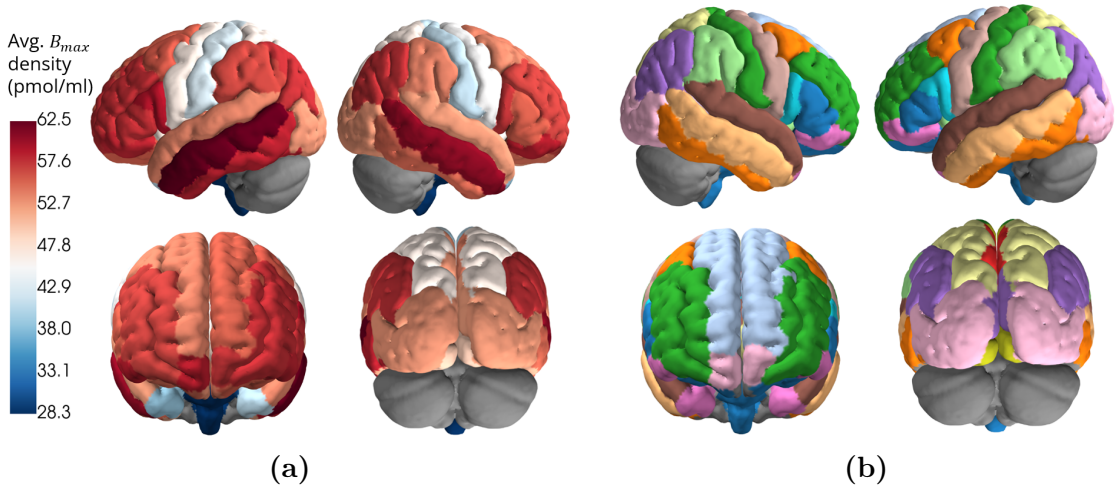

Figure S3: **(a)** 5-HT2A receptor map of average B_{max} densities parcellated into the DK-68 atlas. **(b)** DK-68 atlas displaying each parcel in distinct colors, with homotopic parcels sharing the same color. Excluded areas (i.e., subcortical structures) are displayed in grey.

[*] https://github.com/netneurolab/neuromaps
[†] http://surfer.nmr.mgh.harvard.edu

S.4 Biophysical head model generation

Figure S4 illustrates the process of creating the template head model. The head model was generated from a template T1-weighted image (MNI-ICBM 152 non-linear 2009[‡]. Segmentation was performed with a pre-trained convolutional neural network (based on a stacked 2D U-Net[106]), generating volume masks for the scalp, skull, CSF (including the ventricles), GM and WM. All segmentation masks were manually inspected and corrected as needed. The volume segmentations were then converted to triangulated surface meshes and then to a tetrahedral volume mesh using the SimNIBS library v3.2.3 [§].

The lead field matrix was then calculated for all electrode positions defined in the 10-10 EEG positioning system.[107] This is a $N_{\text{mesh nodes}} \times N_{\text{electrodes}} - 1$ matrix where each column contains the E-field component orthogonal (E_n) to the cortical surface (GM-CSF interface) induced by a bipolar combination of electrodes where Cz is always defined as the cathode (-1 mA). Electrodes were modeled as a cylinder of gel with a height of 3 mm and a radius of 1 cm (representing Neuroelectrics' NG-Pistims[¶]). E-field calculations were performed with the SimNIBS library, assigning to each head tissue an isotropic and homogeneous conductivity: 0.33 S/m, 0.008 S/m, 1.79 S/m, 0.4 S/m and 0.15 S/m, respectively for the scalp, skull, CSF (including the ventricles), GM and WM. The gel representing the electrodes was modeled with a conductivity of 4.0 S/m.

The lead-field matrix was then used to map activity from source space to electrodes using the reciprocity theorem as described in Ruffini (2015).[108] This was performed by first mapping source activity per parcel to activity per mesh node. To do so, initially the activity of a parcel was assigned to all the mesh nodes in the parcel. This initial map was then blurred by applying a linear operator ($\mathbf{B}$) that changes the activity per node to a weighted average of the activity of neighboring nodes, where the weights are determined based on the geodesic distance between nodes and the area of each node of the mesh (defined as the sum of the areas of all the triangles of the mesh that share the node, divided by 3). The electrode voltage differences were then calculated by performing the matrix multiplication of the lead-field matrix and the cortical map of the sources.

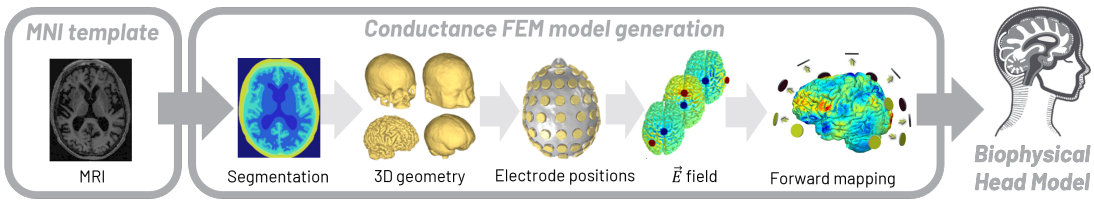

Figure S4: Head model template and cortical mapper generation pipeline. Figure adapted from Salvador et al. (2022)[109]

[‡] https://nist.mni.mcgill.ca/atlases/
[§] https://github.com/simnibs/simnibs
[¶] https://www.neuroelectrics.com/solution/spareparts-consumables/ngpistim

S.5 Uncoupled LaNMM oscillatory behavior

We studied the frequency with the highest PSD (i.e., dominant frequency) in the pyramidal populations over $A_{L5P} \in [0, 10]$ mV, as well as the changes in the membrane potential of P_1 and P_2 resulting from changing the A_{L5P} parameter (Figure S5).

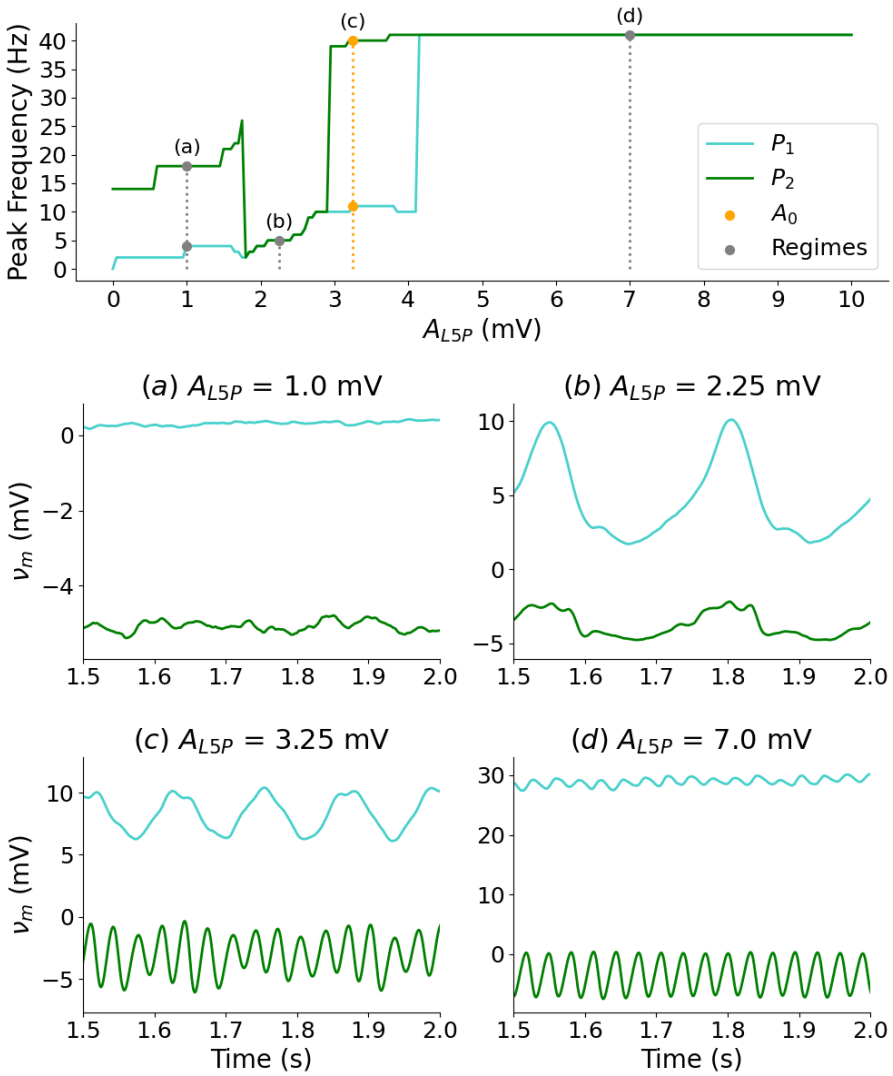

Figure S5: Top: Dominant frequency of the membrane potentials of P_1 (blue) and P_2 (green) pyramidal populations in an uncoupled LaNMM for different values of the synaptic gain A_{L5P} (averaged across five realizations). The orange dashed line denotes the pyramidal gain at baseline A_0 and the grey points denote different model regimes. **Bottom:** Membrane potential of P_1 (blue) and P_2 (green) populations for different A_{L5P} values. The plotted A_{L5P} value is shown on top of each figure. (a) No oscillations regime. (b) Theta/delta oscillations regime. (c) Alpha and gamma oscillations regime. (d) Gamma oscillations regime.

We identify four different dynamical regimes in Figure S5:

1. For $A_{L5P} \in [0, 1.8)$ mV (Figure S5a), no oscillations are present in any pyra-

midal population (noisy regime).

2. For $A_{L5P} \in [1.8, 2.75)$ mV (Figure S5b), theta and delta oscillations are dominant in both pyramidal populations.

3. For $A_{L5P} \in [2.75, 4.15)$ mV (Figure S5c), alpha oscillations are dominant in P_1 and gamma oscillations in P_2 (LaNMM's default regime).

4. For $A_{L5P} \in [4.15, \infty)$ mV (Figure S5d), gamma oscillations are dominant in both pyramidal populations.

To assess whether the spectral power alterations in our model are frequency-specific, we studied the power spectrum of the pyramidal populations over the synaptic gain $A_{L5P} \in [0, 10]$ mV and applied a square window for frequencies $f = [0, 100]$ Hz (Figure S6). The findings show that the area with the highest PSD in P_1 aligns with the delta-theta band for $A_{L5P} \in [2, 2.75]$ mV, the alpha band for $A_{L5P} \in [2.75, 3.75]$ mV, and gamma band for $A_{L5P} > 3.75$ mV. In population P_2, this area lies within the gamma band and agrees with gain values related to gamma oscillations in the previous section. There is also increased PSD in the beta band for both populations, associated with the lower-power harmonics of the alpha band. We conclude that the most significant changes induced by psychedelics in the PSD magnitude in our LaNMM are specific to the alpha and gamma bands within the gain range under study $[A_0, A_{\max}]$ in both P_1 and P_2 populations.

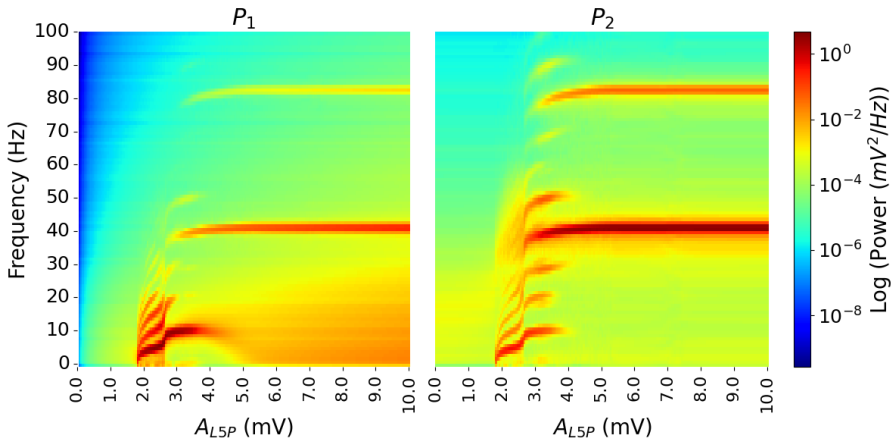

Figure S6: Power spectrum of P_1 (left) and P_2 (right) pyramidal populations membrane potential over A_{L5P} parameter. The PSD (color scale) is shown in a logarithmic scale.

S.6 Whole-brain model fitting results

Figures S7 and S8 show the values of the optimized parameters G and σ_c/σ_i for each subject after model personalization.

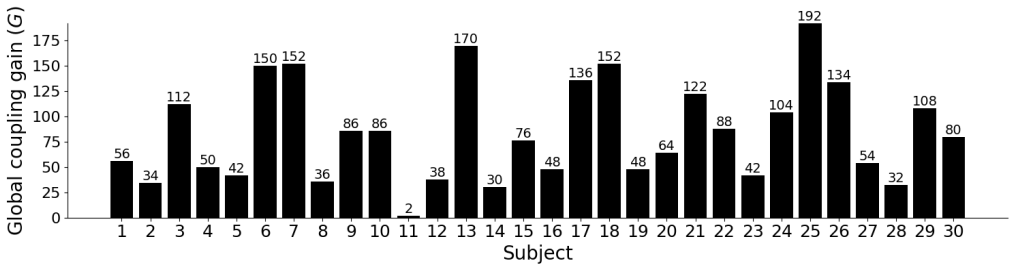

Figure S7: Personalized values of the G parameter after model personalization

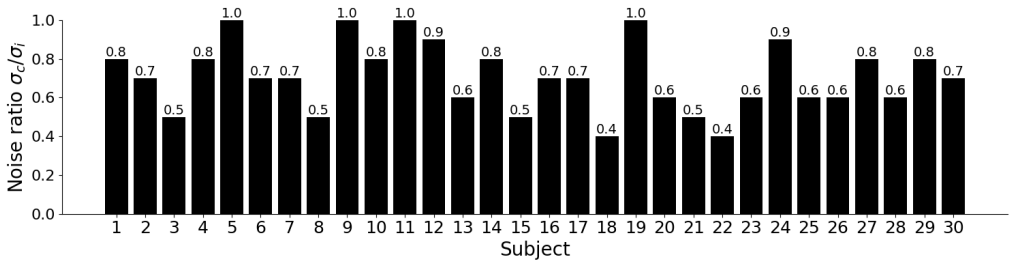

Figure S8: Personalized values of σ_c/σ_i after model personalization

Figure S9 shows the FC matrices obtained from the synthetic BOLD signal for the optimal parameter selection for each subject, compared with the subject's empirical BOLD FC. The optimal value of G and the resulting value of PCC and RMSE between empirical and synthetic matrices is also displayed.

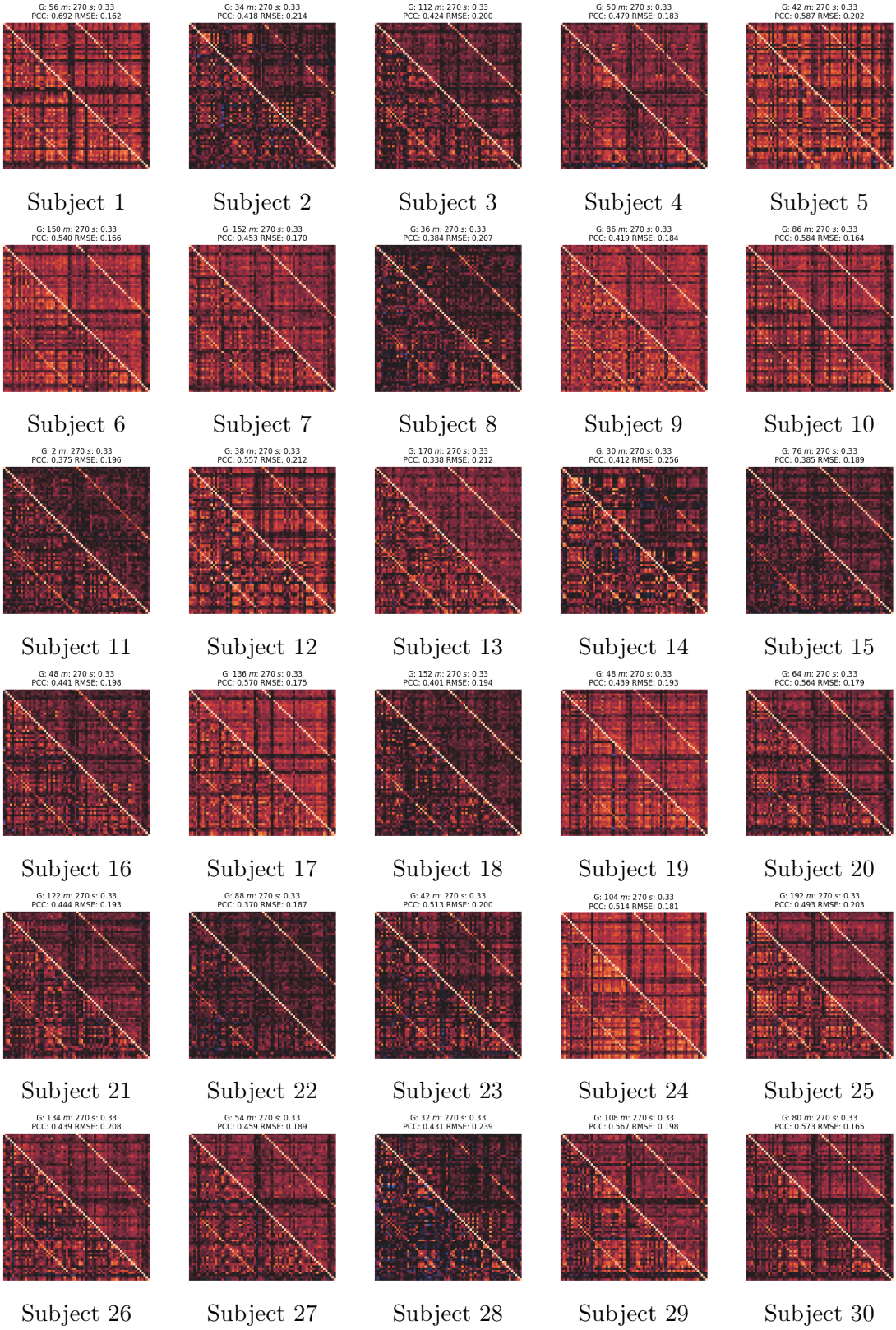

Figure S9: Comparison between the empirical rs-fMRI BOLD FC (lower triangular matrix) and the synthetic FC obtained with the fitted model (upper triangular matrix) for the best set of parameters selected for each subject.